Unstructured CFD Aerodynamic Analysis of a Generic UCAV Configuration

Neal T. Frink
NASA Langley Research Center, Hampton, Virginia 23681 USA

Neal.T.Frink@nasa.gov

Magnus Tormalm
Swedish Defence Research Agency (FOI), 164 90 Stockholm, Sweden

Magnus.Tormalm@foi.se

Stefan Schmidt
Defence Science and Technology Organization (DSTO), Fishermans Bend, Victoria 3207, Australia

Stefan.Schmidt@dsto.defence.gov.au

ABSTRACT

Three independent studies from the United States (NASA), Sweden (FOI), and Australia (DSTO) are analyzed to assess the state of current unstructured-grid computational fluid dynamic tools and practices for predicting the complex static and dynamic aerodynamic and stability characteristics of a generic 53-degree swept, round-leading-edge uninhabited combat air vehicle configuration, called SACCON. NASA exercised the USM3D tetrahedral cell-centered flow solver, while FOI and DSTO applied the FOI/EDGE general-cell vertex-based solver. The authors primarily employ the Reynolds Averaged Navier-Stokes (RANS) assumption, with a limited assessment of the EDGE Detached Eddy Simulation (DES) extension, to explore sensitivities to grids and turbulence models. Correlations with experimental data are provided for force and moments, surface pressure, and off-body flow measurements. The vortical flow field over SACCON proved extremely difficult to model adequately. As a general rule, the prospect of obtaining reasonable correlations of SACCON pitching moment characteristics with the RANS formulation is not promising, even for static cases. Yet, dynamic pitch oscillation results seem to produce a promising characterization of shapes for the lift and pitching moment hysteresis curves. Future studies of this configuration should include more investigation with higher-fidelity turbulence models, such as DES.

1.0 NOMENCLATURE

b = wing span, =1.54m
C_L = lift coefficient, =Lift/$q_\infty S_{ref}$
C_m or CM = pitching moment coefficient, =Pitching_Moment/$q_\infty S_{ref}\, c_{ref}$
C_p = pressure coefficient
c_{ref} = reference chord, =0.479m
c_{root} = wing root chord, =1.06m
f = sinusoidal oscillation frequency about pitch, roll, or yaw axis, Hz.
k = wind tunnel test reduced frequency, $=2\pi f \cdot c_{ref}/U_\infty$
$log(r/r0)$ = order of magnitude drop in solution residual, e.g. -4 means 4 orders of magnitude drop

M_∞ = freestream Mach number, =0.144
MRP = Moment Reference Point for pitching moment, =0.600m from apex
N_θ = Number of time steps per oscillation cycle, $=2\pi/(k \cdot \Delta t^*)$
p = static pressure, Pascal (Pa)
RRP = Rotational reference point for pitch and yaw oscillation, =0.855m from apex
Re_{cref} = Reynolds number based on c_{ref}, =1.6 million
rate1 & rate2 = primary& secondary VGRID viscous stretching factors, see Eq. 1
S_{ref} = reference area, $=0.77\text{m}^2$
s/LE = fractional distance from wing apex along wing leading edge
T = temperature, degK
Δt = physical time step, seconds
Δt^* = characteristic time step, $=\Delta t \cdot U_\infty / c_{ref}$
U_∞ = freestream velocity, =50m/s
x,y,z = model coordinates, mm (see Figure 2)
α = angle of attack ($\alpha=\alpha_0 \pm \Delta\alpha$), deg.
α_0 = nominal angle of attack for pitch oscillation, deg.
$\Delta\alpha$ = range of pitch oscillation about body axis, +/-deg.
β = angle of sideslip, deg.
δ_{i+1} = VGRID viscous grid spacing normal to surface at node $i+1$, see Eq. 1, meter
δ_1 = spacing of first node off of surface ($i=1$) in viscous grid layers, see Eq. 1, meter
μ = laminar viscosity, kg/(s·m)

Key Acronyms

ARSM = Algebraic Reynolds Stress Model
CPU = Central Processing Unit (measure of computer resource usage), hours
DES = Detached Eddy Simulation turbulence model
DDES = Delayed Detached Eddy Simulation turbulence model
DSTO = Defence Science and Technology Organisation, Australia
DNW-NWB = German-Dutch Wind Tunnel located in Braunschweig
EARSM = Explicit Algebraic Reynolds Stress Model
FOI = Swedish Defence Research Agency, Sweden
LE = Wing leading edge
LES = Large Eddy Simulation
MPM = Model Positioning Mechanism in the DNW-NWB wind tunnel
NASA = NASA Langley Research Center, United States
NATO/RTO = North Atlantic Treaty Organization, Research Technology Organization
PIV = Particle Image Velocimetry
RK = Runge Kutta
SA(O) = Spalart-Allmaras (Original) one equation turbulence model
SARC = Spalart-Allmaras model with rotation correction term
SST = Menter's Shear Stress Transport two equation turbulence model
TE = Wing trailing edge
UCAV = Uninhabited combat air vehicle
(U)RANS = (Unsteady) Reynolds Averaged Navier Stokes

2.0 INTRODUCTION

Historically, many civil and military aircraft development programs have encountered critical stability and control (S&C) deficiencies during early stages of flight test despite thousands of hours of wind tunnel testing. These surprises have occurred across the speed range from takeoff and landing to cruise flight, and particularly at the fringes of the flight envelope where separated flows dominate. It has been widely believed within the research community that the next significant improvement in the state of the art for predicting the S&C characteristics of a new vehicle might be through the application of computational fluid dynamics (CFD) tools. Applying high-end CFD codes with a Reynolds-averaged Navier Stokes (RANS) or better level of technology to specific areas of S&C interest before first flight can help focus the wind tunnel program and provide improved understanding of the underlying flow physics. When S&C parameters are determined by wind tunnel or CFD methods, the basic principle is to determine forces and moments on an aircraft when it is undergoing oscillations in pitch, roll, or yaw. While S&C problems most commonly occur near the margins of the flight envelope, the computational solution of S&C for even steady flight conditions can be demanding. Fortunately, a critical mass of international researchers has been assembled to address this challenge through the North Atlantic Treaty Organization (NATO) Research Technology Organization (RTO).

In 2007, a 3-year international collaboration was initiated thorough the NATO/RTO AVT-161 Task Group titled "Assessment of Stability and Control Prediction Methods for NATO Air & Sea Vehicles" to investigate the applicability of current CFD tools for predicting S&C characteristics of air and sea vehicles. The specific objectives were to 1) assess the state-of-the-art in computational fluid dynamics methods for the prediction of static and dynamic stability and control characteristics of military vehicles in the air and sea domains, and 2) identify shortcomings of current methods and identify areas requiring further development including aspects of computational uncertainty. As summarized in Ref. [1], the AVT-161 team made remarkable progress through the leveraged efforts of many engineers and researchers from 19 organizations in 9 countries by 1) conceiving a generic uninhabited combat air vehicle (UCAV) focus configuration called **S**tability **a**nd **C**ontrol **Con**figuration (SACCON), 2) designing and building the wind-tunnel model, 3) conducting two test entries in Germany and one in the United States, and 4) conducting and coordinating several multi-national computational studies between researchers from 9 countries. The AVT-161 team met twice per year in NATO host countries and collaborates as needed between meetings.

Initial team efforts were focused on computing and understanding the static and dynamic aerodynamic characteristics of the SACCON configuration, which was a challenge because of the complexity of the flow field. A summary of its aerodynamic characteristics is presented in Ref. [2]. Experimentalists within the AVT-161 team have conducted both static wind-tunnel tests and dynamic tests on the SACCON configuration undergoing pitch, roll, and yaw oscillation to measure the dynamic stability and aerodynamic characteristics [3-6]. The prevalent experimental methodology for quantifying the dynamic stability of an aircraft calls for extracting the dynamic stability derivatives from the force and moment coefficients as the aircraft undergoes a periodic motion about a body axis in a wind tunnel. Other team members are running parallel dynamic computational studies following a similar approach of modelling SACCON undergoing pitch, roll, and yaw oscillation with their respective CFD tools [7-13]. The collective experiences from these studies have confirmed the difficulty of achieving accurate and efficient computation of dynamic stability characteristics. Furthermore, they affirmed the necessity of understanding the particular nuances of each particular CFD grid and flow solver before broad application of the tools to this class of problem.

This article summarizes the results of three studies from the United States, Sweden, and Australia[1] [7,9] conducted with unstructured-grid methodologies. The work reflects the status of the respective set of SACCON computations at the end of the AVT-161 task group, and thus offers guidance for future studies. The paper is organized with a description of the SACCON Geometry and Experiment in Section III. The computational tools used by the three authors are described in Section IV. The respective approach employed by each organization to apply its specific computational tool for both static and dynamic simulations is described in Section V. Finally, the collective results from the three studies are presented and analyzed in Section VI. From this, an attempt is made to understand the key strengths and limitations of applying

---

[1] In addition to the participating NATO members, Sweden (FOI) and Australia (DSTO) were also invited to join the task group.

unstructured-grid methodologies for computing the aerodynamic characteristics on a configuration exhibiting complex vortical flow interactions for static conditions and under forced oscillating motions.

3.0 GEOMETRY AND EXPERIMENT

The SACCON geometry depicted in Figure 1 is described in detail in Ref. [1]. It is a generic representation of a UCAV configuration with 53-deg swept leading-edge that can be tested either sharp or rounded. The configuration of interest to this study is designated the SACCON_01 round-leading-edge (RLE) configuration, which has a sharp inboard leading edge segment that transitions to a medium round leading edge on the outer wing panel. The outer wing panels are twisted about the leading edge to yield a 5-deg washout. As shown in Figure 2, the wingspan b=1.54m, root chord c_{root}=1.06m, and reference chord c_{ref}=0.48m. The reference area S_{ref}=0.77m^2. The rotation reference point for pitch and yaw oscillation, $RRP[x,y,z]=[0.855,0,0]$m, is positioned near the aft end of the root chord, downstream of the aerodynamic moment reference point, $MRP[x,y,z]=[0.6,0,0]$m. The wind-tunnel model was designed to accommodate a belly sting attached at the *RRP* for tests in the German-Dutch Wind Tunnel (DNW-NWB) located in Braunschweig, Germany as shown in Figure 1, or a rear sting mount for the NASA Langley 14- by 22-Foot Subsonic Tunnel in Hampton, Virginia, United States.

The SACCON wind tunnel model is constructed from lightweight composite material to facilitate dynamic oscillation testing. It is equipped with more than 200 pressure taps on the upper and lower surface of the model (Figure 3) that are configured for dynamic measurement of unsteady pressures. The surface was painted with shiny black paint that contains particles of Rhodamine B to reflect laser light at a different wavelength, which can be filtered so as to produce highly accurate PIV measurements close to the surface [5,6]. Both static and dynamic PIV measurements were obtained.

For the CFD comparisons to follow, the static and dynamic experimental data were obtained in the DNW-NWB low speed tunnel [3,4], shown in Figure 1, at sea level atmospheric conditions at freestream velocity $U_\infty=50$m/s, Mach number M_∞=0.149, and chord Reynolds number Re_{cref}=1.6 million. Static measurements covered an angle of attack (α) range from 0 to 30 deg, and sideslip sweeps of β=±10 deg. Dynamic data was measured for sinusoidal pitch oscillation of $\Delta\alpha$=±5 deg about α_0=0, 10, 15, and 20 deg with frequencies (f) of 1, 2, and 3 Hz which corresponds to reduced frequencies ($k = 2\pi f \cdot c_{ref} / U_\infty$) of 0.06, 0.12, and 0.18, respectively. Yaw and roll oscillation data are also available, but not used in this study.

Initial tests with the SACCON_01 RLE configuration revealed an arbitrary boundary layer transition line on the upper surface of the model detected by infrared thermography. This discovery led to a decision to apply carborundum trip grit to fix transition near the leading edge. Transition of the boundary layer to fully turbulent flow was subsequently verified with the infrared thermography [1,3].

4.0 COMPUTATIONAL TOOLS

4.1 Grid Generators

4.1.1 VGRID (NASA)

VGRID [14,15] is a tetrahedral grid generator based on the Advancing Front Method (AFM) for generation of surface triangles and 'inviscid' field cells, and the Advancing Layers Method (ALM) for generation of thin-layered 'viscous' cells. Both techniques are based on marching processes in which tetrahedral cells grow from an initial front (triangular surface mesh) until the volume around the geometry is filled. Unlike the conventional AFM, which introduces cells into the field in a totally unstructured manner, the ALM generates organized layers of thin tetrahedral cells, one layer at a time, while maintaining the flexibility of AFM. Once the advancing front process is completed in VGRID, an additional post-processing step is required using POSTGRID to close any open pockets and to improve grid quality. VGRID input files are generated by an interactive geometry manipulation program, GridTool [16]. This graphics tool can import surface definitions from Initial Graphics Exchange Specification (IGES) files containing Non-Uniform Rational B-Spline (NURBS) surfaces and curves, as well as PLOT3D point definition files. GridTool is used to manipulate the geometry and to define necessary geometric surface patches and grid-spacing (source) parameters. It uses OpenGL for 3D graphics, and is available for Mac and Linux systems. The graphical interface is based on the Fast Light Toolkit.

4.1.2 ICEM CFD™ and TRITET (FOI and DSTO)

Multiple grid generation tools were used in the FOI and DSTO studies. ANSYS® ICEM CFD™ Tetra and a combination of ICEM CFD™ and TRITET served as the two grid generation methods. ICEM CFD™ Tetra is able to generate meshes using a variety of techniques such as the Delaunay, Advancing Front, and Octree mesh methods [17]. The Octree method was used for the FOI and DSTO meshes and is briefly described here. Starting from an all encompassing root tetra element (based on a global size specification), Tetra subsequently refines the elements until all surface size requirements are met limiting size differences of cells sharing an edge or surface to less than two. After that ICEM CFD™ Tetra adjusts node locations and makes sure that adjacent elements share an entire face. Assuming a water-tight geometrical model, Tetra then cuts away the unused mesh parts and finishes off by moving and merging nodes as well as swapping edges to improve the overall mesh quality (i.e. aspect ratios). ICEM CFD™ Prism is used to add prism layers after the surface or volume mesh has been generated. Each prism layer can then be generated individually or as a thick single prism layer, which can be split into the desired number of layers specifying either the initial height or the stretching factor.

The second mesh generation process consists of two steps. In the first step, an inviscid tetrahedral mesh is generated and smoothed using ICEM CFD™ Tetra, as described previously. The inviscid mesh is then used as background input to the second step using the FOI developed mesh generator TRITET [18]. ICEM CFD™ Tetra has a better ability to handle common geometry format. The predominant geometric input of TRITET is structured surface patches that are difficult to define for a complex model. However, in this study TRITET directly utilized the triangular surface mesh from ICEM CFD™ Tetra to start building the prismatic boundary layer normal to the walls. TRITET is based on the advancing front algorithm that offers the user good control of the distribution of the prismatic layers as well as corners. The number of added layers depends on user input or the element size of the inviscid background mesh. TRITET stops adding prismatic elements in areas where the size matches that of the tetrahedra in the outer mesh to allow a smooth volumetric transition. The final inner volume is also generated in TRITET using the advancing front technique and rebuilds the volume mesh while respecting the size of the original inviscid background mesh.

4.2 Flow Solvers

Two unstructured Navier-Stokes flow solvers based on fundamentally differing methodologies are exercised among the three computational studies. For the NASA application, the USM3D code solves the flow equations at tetrahedral cell centers, whereas the FOI EDGE code solves them at vertices or nodes of general cell topologies. The principle impact is that on a given tetrahedral grid, there are between 5 and 6 times more cells than nodes, and twice as many surface triangles than surface nodes. Hence on a full tetrahedral grid, the node-centered method will require a finer grid than that needed by a cell-centered code to achieve comparable spatial resolution of the field solution. The impact of these differences is significantly softened for the FOI and DSTO grids through finer field-grid resolution and by exploiting the use of prismatic cells across the boundary layer.

4.2.1 USM3D Solver (NASA)

The NASA computations are performed with the USM3D flow solver [19] that is part of the NASA Tetrahedral Unstructured Software System (TetrUSS) [20]. USM3D is a parallelized tetrahedral cell-centered, finite volume compressible RANS flow solver. The term cell centered means that the finite volume flow solution is solved at the centroid of each tetrahedral cell. Inviscid flux quantities are computed across each tetrahedral cell face using various upwind schemes. Spatial discretization is accomplished by a novel reconstruction process, based on an analytical formulation for computing solution gradients within tetrahedral cells. The solution can be advanced in time by a 2^{nd}-order physical time step scheme, a 2^{nd}-order dual time step scheme [21], or to a steady-state condition by an implicit backward-Euler scheme. Several turbulence models are available [22]: the one-equation Spalart-Allmaras (SA) model, and several two-equation models by Jones and Launder k-ε model, Menter Shear Stress Transport (SST) model, two nonlinear Algebraic Reynolds Stress Models (ARSM) of Girimaji and Shih/Zhu/Lumley, and the Wilcox 1988 k-ω model. Detached Eddy Simulation (DES) has been implemented in all of the turbulence models [21]. A capability to trip the flow at specified locations on aerodynamic surfaces has been implemented for the k-ε turbulence model, but fully turbulent flow is assumed for the results to follow. USM3D has capabilities for overset grids and dynamic grid motion, the latter being utilized in the current study.

4.2.2 EDGE Solver (FOI and DSTO)

The flow solver EDGE [23] is primarily developed and maintained by FOI. Since the start of the EDGE project in 1997, several academic and research institutes have joined the EDGE community as users and developers. In Sweden, the main users are Saab Aerosystems and The Royal Institute of Technology, KTH. EDGE is available as a complete source package, subject to the FOI license agreement.[2]

EDGE solves the three dimensional RANS compressible flow equations on general unstructured grids using an edge-based data structure and node-centered finite volume technique. The edge-based formulation makes it easy to compute any type of element, structured or unstructured. The control volumes are non-overlapping and are formed by a dual grid, which is computed from the control surfaces for each edge of the primary input mesh. In any EDGE mesh, all the mesh elements are connected through matching faces. EDGE meshes therefore may not contain hanging nodes.

In the flow solver, the governing equations are integrated explicitly towards steady state with Runge-Kutta (RK) time integration. Convergence is accelerated using agglomeration multigrid and implicit residual smoothing. Time accurate computations can be performed using a semi implicit, dual time stepping scheme that exploits convergence acceleration technique via a steady state inner RK iteration procedure. Every program in the EDGE system can be accessed and executed via a command-line interface, which is implemented as set of simple Unix shell scripts. However, there is also a platform-independent graphical user interface (GUI) written in Java.

A variety of turbulence models are available, which are categorized into three different groups, RANS, DES and Large Eddy Simulation (LES) models. The RANS model includes the original one-equation model by

---

[2] A limited binary version is available for free download at www.foi.se/edge.

Spalart-Allmaras (SAO), and several two-equation models: the Menter SST and Baseline (BSL) models, the Wilcox 1988 k-ω model, the Wallin and Johansson Explicit Algebraic Reynolds-Stress Model (EARSM) [24] implemented within the Hellsten k-ω model, and a Differential Reynolds Stress Model (DRSM). The DES extension is implemented with the SA model (DES-SA), the Peng hybrid RANS-LES model, and the LES models of Yoshizawa and Smagorinsky.

Recent development in EDGE includes flow control in the form of vortex generators and micro-jets, aeroelastic coupling with FOI developed computational structural mechanics code, Stripe, and an adjoint solver for shape optimization.

5.0 COMPUTATIONAL APPROACHES

NASA, FOI, and DSTO each performed their computational studies independently [7,9] using internally developed practices. A primary difference to note between approaches is that the geometric representation in the NASA grids included the 105-deg support sting with the SACCON model, whereas the FOI and DSTO grids did not include a support sting. Also, the NASA solutions were generated on full tetrahedral grids with a cell-centered methodology, whereas FOI and DSTO utilized hybrid grids containing prisms/pyramids/tetrahedra with a vertex-based solution methodology. The following describes their respective approaches to grid generation and flow solution strategies.

5.1 Grid Generation

A total of seven computational SACCON grids were utilized among the three organizations. Their general mesh properties are compared in Tables 1 and viscous grid properties in Table 2. The bold entries in Table 1 emphasize the relevant metrics for mesh size pertinent to the cell- or node-based flow solvers used by the respective organizations. For reference purposes in Table 1, the metrics of a half-span equivalent to the full-span FOI Basic grid are included in parenthesis. The details of each grid are described in the following subsections.

Table 1: General mesh properties for SACCON grids

Org	Grid	Span	Sting	Max LE/TE Strething	Nodes	Prisms	Pyramids	Tets	Wing triangles	Wing nodes
NASA	Grid 1	Half	Y	10-to-1	604,111	0	0	**3.51M**	**36,661**	18,333
	Grid 2	Half	Y	10-to-1	1.08M	0	0	**6.30M**	**66,549**	33,277
	Grid 3	Half	Y	10-to-1	2.15M	0	0	**12.53M**	**131,194**	65,599
	Grid 1.1	Half	Y	1-to-1	1.54M	0	0	**9.02M**	**123,431**	61,718
FOI	Basic	Full	N	1-to-1	**5.49M**	9.42M	135,703	3.91M	162,686	**292,693**
		(Half)[3]	N	1-to-1	**(2.74M)**	(4.71)	(67,852)	(1.96)	(81,343)	**(146,346)**
	Adapted	Half	N	1-to-1	**23.0M**	31.9M	211,337	39.3M	568,802	**1.10M**
DSTO	P3h	Half	N	1-to-1	**10.3M**	9.18M	104	2.47M	256,729	**459,127**

---

[3] Metrics for half-span equivalent to the full-span Basic grid.

Table 2: Viscous characteristics of SACCON grids

Org.	Grid	No. BL Layers	1^{st} cell height, mm	Expansion factor	Avg. y^+	Typical surface triangle size along LE, mm	
						Spanwise	Chordwise
NASA	Grid 1	72 tets (24 nodes)	0.003	1.15	0.4_{cell}	6.5	0.75
	Grid 2		0.003	1.15	0.4_{cell}	4.7	0.5
	Grid 3		0.003	1.15	0.4_{cell}	3.4	0.4
	Grid 1.1		0.003	1.15	0.4_{cell}	0.75	0.75
FOI	Basic	50 nodes (50 prism)	0.001	1.2	0.2_{node}	0.5	0.45
	Adapted	40 nodes (40 prisms)	0.004	1.2	0.7_{node}	0.35	0.3
DSTO	P3h	15 nodes (15 prisms)	0.010	1.35	1.5_{node}	0.2	0.2

5.1.1 NASA Grids

Four half-span tetrahedral grids were generated for the SACCON_01 RLE configuration with the 15-deg yaw link on the 90-deg post support sting (referred to as the 105-deg sting) using the tetrahedral unstructured grid generation tools GridTool and VGRID. A developmental version of VGRID [15] was used for grids in the present study. Thin-layer tetrahedral grids were generated to meet requirements for cell-centered computations from the USM3D flow solver. A near-wall first-cell spacing was prescribed, based on flat-plate turbulent boundary layer theory, to achieve a tetrahedral cell centroid turbulent wall coordinate (y^+_{cell}) of *0.5* at a longitudinal distance of $0.5*c_{ref}$ for a Re_{cref}=1.6 million. Since layers of nodes march away from the vertices of the surface triangles with the Advancing Layers Method, an initial VGRID spacing, δ_1, corresponding to a $y^+_{node}=2$ at the first node was prescribed in order to achieve the $y^+_{cell}\approx 0.5$ at the first cell centroid[4]. Subsequent USM3D computations confirmed that an average cell-centered $y^+_{cell}=0.42$ was achieved. For the SACCON at the wind tunnel chord Reynolds number of 1.6 million, the required VGRID first-node spacing is $\delta_1/c_{ref}=2.4E\text{-}05$, and expansion factors of $rate1=0.15$ and $rate2=0.02$, where the nodal spacing layers are defined by the Eq. (1).

$$\delta_{i+1} = \delta_1 \cdot [1 + rate1 \cdot (1 + rate2)^i]^i \tag{1}$$

The same viscous spacing distribution was applied to all four grids and resulted in approximately 72 tetrahedral cells (24 nodes) across the boundary layer at the mid-chord of c_{ref}.

The characteristics of the NASA grids are summarized in Tables 1 and 2, and visualized in Figure 4. The grid refinement was achieved by changing a global scaling parameter in the VGRID input, which only impacts the inviscid portion of the grid. The normal distributions across the viscous layers were not scaled by this parameter. Spanwise grid stretching with a ratio as high as 10-to-1 was applied along the leading- and trailing-edges (LE, TE) for Grids 1, 2, and 3, as evidenced in the surface triangulation depicted near the wing-apex/symmetry-plane juncture in Figure 4(a-c). A fourth Grid 1.1, also detailed in Figure 4(d) was generated by turning off the spanwise stretching parameter in the VGRID input file for Grid 1. The resulting isotropic Grid 1.1 had 2.6 times more cells than Grid 1, which highlights the benefits of grid stretching to reduce cell

---

[4] The ALM forms layers of prismatic cells that are each sub-divided into three tetrahedral cells. The distance from the surface to the centroids of the tetrahedral boundary cells is one-fourth that of the first layer of nodes, resulting in $y^+_{cell} = 0.25 \cdot y^+_{node}$.

count. The farfield boundaries were defined as a box, extending approximately 24 root chords from the wing in all directions.

5.1.2 FOI Grids

Two unstructured grids were generated by FOI on the SACCON geometry without the support sting. The ANSYS® ICEM CFD™ code was used to generate the triangular surface mesh and an initial tetrahedral volume mesh. The farfield was modeled as a squared box, approximately 50 root chords, away in all directions. The blunt trailing edges have been coarsely resolved with 1 to 4 elements. More care was taken at the leading edges to achieve the dense mesh needed to resolve the typical shear layer roll up of delta wings. Also the anticipated vortical flow area above and behind the model was refined initially using density boxes seen in Figure 5. The mesh was smoothed in ICEM CFD™ before being transferred into the TRITET mesh generator to grow the viscous layers.

Several FOI meshes were created but only two are presented in this article; a Basic full-span mesh and a solution-adapted half-span mesh shown in the left and center columns of Figure 5, and in Tables 1 and 2. The full-span Basic mesh consists of 5.5 million nodes and was used both for the static and dynamic simulations. A very fine resolution of the boundary layer was made for the Basic mesh. A maximum of 50 prismatic layers with an initial height of 0.001mm, expansion ratio of approximately 1.2 and a maximum height of 80 mm were specified. Initial calculations showed y^+_{node} values well below one on a typical flow case with Reynolds number of 1.6·million. The statistics for a half-span equivalent to the full-span Basic grid are included in Table 1 to facilitate comparisons with the other grids.

The solution adapted mesh having 23 million nodes was constructed with the h-refinement routines in TRITET, which could be made available as part of the EDGE package. The Adapted mesh was only used for the static cases. The standard feature-based h-refinement sensor that combines the influence of all primitive variables was applied with a constraint of minimum cell size, 0.001mm, to subdivide the affected tetrahedra into 2, 4 or 8 new tetrahedron. The prismatic elements were also refined. New surface nodes were projected using the spline function. Since the Basic mesh had revealed rather low values of y^+_{node}, the first cell height was increased to 0.004mm and the number of prismatic layers was reduced down to 40. This makes the Adapted grid coarser in the wall normal direction. The adaption was accomplished in two steps. An initial fine half mesh of 5 million nodes (not shown here) with a RANS solution at α=17 deg, M_∞=0.15, Re=1.6·million was used by TRITET for the first h-refinement, resulting in an 11 million node mesh. A second RANS solution, also at α=17 deg, was calculated on the first adapted mesh and used for the second and final h-refinement. Both the Basic and the final Adapted mesh are compared in Figure 5. Note that the symmetry plane in the Basic mesh has been cut from a full span mesh, thereby giving the impression of a more dense mesh is some areas. Note also the high density of nodes away from the body for resolving the vortical flow structures.

5.1.3 DSTO Grid

The DSTO mesh, designated P3h, is compared to the two FOI meshes in the right column of Figure 5, and with all meshes in Tables 1 and 2. An initial half-span surface and volume mesh was created for the P3h with ANSYS® ICEM CFD™ using the Octree option. Then ICEM CFD™ Prism was used to add near-wall prism layers into the existing volume mesh. Once the prism layers are complete, and the prism and tetrahedral cells merged, the mesh is smoothed. The boundary layer was modeled with 15 prism layers yielding a total height of about 2.5mm based on a stretching factor of 1.35. Resulting average y^+_{node} values were typically in the range of 1.5. Mesh points were concentrated at the leading edge using a linear density region and on the upper wing surfaces. The tip is resolved by 5-6 cells while the trailing edge is resolved by only 2 cells, with this area being of lesser importance compared to the other regions at least for lower angle-of-attacks. Despite the prism layers and added tetrahedra on the upper surface, off-body resolution is still limited, which posed difficulties in the current study with resolving the dominant vortical structures above the upper wing surface.

The P3h mesh was originally developed for another numerical study of SACCON static aerodynamics and dynamic stability derivatives [13] that utilized the cell-centered unstructured flow solver, COBALT, which has different grid requirements than node-centered solvers. A strong consideration was given to minimizing the mesh cell count in order to achieve reasonable solution CPU times for establishing the processes of running dynamic stability cases. Additional computations, summarized herein, were performed on this mesh by DSTO using the node-centered EDGE code as a part of a larger exploratory effort by the AVT-161 task group to establish guidelines for simulating the SACCON aerodynamics and flow field. Although the following results will demonstrate this grid to be under resolved in the field for a node-centered solver, they reflect an important contribution by DSTO to the AVT-161 task group in establishing lower boundaries of grid resolution.

5.2 Flow Solution Strategy

5.2.1 NASA Solutions

USM3D solutions are generated using an implicit 2nd-order physical time-step scheme for both the static and dynamic cases. The details of prescribing the time steps and subiterative convergence will be discussed in the Section VI. Inviscid fluxes are computed with Roe's Flux Difference Scheme without limiting. The time-accurate or unsteady RANS (URANS) flow solutions are predominately computed with the SA turbulence model. Limited assessments are also made for the static cases with the SST, k-ω, and ARSM turbulence models, and for the dynamic cases with the SST model. The boundary conditions consist of a surface no-slip condition on the wing and support sting, a symmetry condition on the symmetry plane, and characteristic inflow/outflow on the outer box. The forced-oscillation solutions are generated using non-deforming solid-body rotation of the full grid about the spanwise axis through the aft-body near the sting, and initialized by restarting from a converged static solution at the prescribed angle of attack, α_0, and cycled for two full oscillations of ±5 deg. However, the hysteresis of forces and moments is converged to its periodic solution after the first ¼ cycle of oscillation.

5.2.2 FOI Solutions

The EDGE solutions are generated with an explicit 3-stage Runge-Kutta (RK) scheme for the static cases, and the 2nd-order implicit dual time step scheme with inner RK iterations for the dynamic cases. The convergence is accelerated using agglomeration multigrid (3 levels) and implicit residual smoothing. Inviscid fluxes are computed with the 2nd-order spatial accurate central differencing discretization scheme with artificial dissipation. The FOI RANS and URANS solutions in this study are computed with the EARSM turbulence model. The detached eddy simulations are computed using DES-SA and implicit dual time stepping. All cases are calculated as fully turbulent, with the default free stream turbulence intensity of 0.1%. The far-field boundary used a weak characteristic condition, specifying the static pressure, static temperature and flow velocities. The values were taken from the actual wind tunnel test data as presented in Ref. [3,4]. The solid surfaces were specified as an adiabatic no-slip wall and a symmetry condition was applied on the half-span Adapted mesh.

Typical EDGE RANS solutions on the Basic grid were generated with 6000 iterations on eight parallel processors. A single iteration took 45s. The Basic-grid solution residuals exhibited a high degree of oscillation, especially for higher angle of attack. The more demanding cases with the Adapted mesh were started on 24 processors. Approximately 10000 iterations were required for the Adapted-grid RANS solution, producing a much more stable convergence compared to the Basic-grid RANS. The Adapted-grid RANS simulations required 85s to run per iteration on 24 processors. Force and moment comparisons are made with mean-flow averages of the coefficients collected during the final 200 iterations.

The Basic-grid DES-SA calculations were initiated from the RANS solutions. Despite the heavily oscillating convergence of Basic-grid RANS solution, the DES-SA modeling stabilized the residuals. In most cases, initial transients damped out after 200-300 time steps. The Basic-grid DES cases were run for 500 time steps of Δt=0.0005s (Δt^*=0.053 where $\Delta t=\Delta t^* \cdot c_{ref}/U_\infty$) and 40 inner iterations in the dual time step cycle. Each inner iteration required 40s on eight parallel processors. Thus, a total simulation time of 1800 CPU hours per case were used. For most of the Basic-grid DES-SA simulations, the flow analysis was made on the mean flow field collected during the final 100 time steps. Some cases presented here were iterated even further. The Adapted-grid DES-SA simulations required 20-times more computer resource than the Basic-grid RANS case. The lowest acceptable number of time steps was between 600 and 800 steps. A mean-flow average of the coefficients was collected during the final 200 time steps.

The dynamic forced oscillation simulations were conducted with the URANS approach on the FOI Basic grid. The time step was prescribed to yield 100 steps per pitch cycle for the f =1Hz and 3Hz cases. Initial calculation revealed a slow inner convergence between time steps. The maximum number of inner iterations was increased to 200 to allow an acceptable inner convergence of the integrated forces.

Prescribed mesh movement for the forced oscillation solutions was accomplished with a modal mesh movement capability that is embedded in the EDGE aero-elastic routines. Functions within the EDGE package are used to create two additional meshes at the extremes of the pitch oscillation cycle, $\alpha=\alpha_0 \pm \Delta\alpha$. Deformed meshes are created by calling a number of functions in the EDGE package before the pre-processor step. At each time step during an EDGE run, a linear interpolation is made between baseline and rotated meshes to find the intermediate mesh position based on the prescribed motion. The motion is pre-defined by a time series in a control file. The linear interpolation of mesh points between the baseline and rotated meshes result in a small error. However, for these relatively small angles, around 5 degrees, the error was considered to be acceptable.

For all FOI static computations, the Message Passing Interface (MPI) compilation of EDGE 4.1 (revision 1903) was used on FOI's Linux Intel XEON®- and AMD Opteron-based cluster, Tunnan. The dynamic simulations have been computed with the later release EDGE 5.0 (revision 2086). A verification study confirmed that no differences occur in computed results between version 4.1 and 5.0. Recent additions and upgrades with Infiband interconnect have increased the capacity to 1150 processors and improved computational speed on individual nodes by 30- to 40-percent.

5.2.3 DSTO Solutions

DSTO exercised the EDGE solver with three turbulence models. Two were based on the Spalart-Allmaras one-equation model and the third on the Menter SST two-equation model. The Strain-Adaptive Linear Spalart–Allmaras (SALSA) model of Rung [25] was implemented into EDGE by DSTO for its ability to account for moderate non-equilibrium effects and improved near-wall behaviour, which increases the robustness hence convergence for industrial applications. The extension of the SALSA model is achieved by a modification of a model constant (*Cb1*) in the original SA formulation (SAO) that sensitizes the production term to non-equilibrium effects by reducing the anisotropy parameter with respect to the strain rate.

Inviscid fluxes were computed in EDGE using a 2nd-order spatially accurate central differencing scheme with artificial dissipation. The steady state solutions were advanced using an explicit 3-stage Runge-Kutta scheme with convergence accelerated by agglomeration multigrid (3 levels) and implicit residual smoothing. It was determined through experimentation that 16,000 iterations were needed for adequate solution convergence of the complex flows around SACCON.

6.0 RESULTS

6.1 Static Aerodynamics

NASA, FOI, and DSTO have computed static aerodynamic results for the cases in Table 3 using the USM3D and EDGE flow solvers for comparison with the DNW-NWB wind tunnel data [3]. Fully turbulent flow was assumed for all computational results. The model support sting is included in the NASA representation, and not included in the FOI and DSTO representations. Full tetrahedral grids are used for the NASA/USM3D study, and hybrid prism/pyramid/tetrahedral grids for the FOI and DSTO EDGE studies. Additional solutions were generated using DSTO/EDGE with the four NASA grids and conditions to supplement the following analysis. Slight differences can be noted for the particular angles of attack in Table 3 between the NASA and FOI, DSTO cases. These static results are used to 1) provide characterization of the highly non-linear flows to be encountered by SACCON, and 2) illuminate the aerodynamic sensitivities for the various flow solvers and grids. All force and moment (F&M) coefficients are integrated over the wing aerodynamic surface (sting excluded) and are referenced to wing area S_{ref} =0.770m^2, chord c_{ref}=0.479m, and moment reference point, *MRP*[*x,y,z*]=[0.6, 0, 0]m.

Table 3: Common static test cases, wind tunnel conditions (TN2373, VN1406 [3])

Parameters	Conditions
Model Positioning Mechanism (MPM)	15-deg yaw link (105-deg sting)
Static Pressure, p	97767 Pa
Static Temperature, T	291.2 K
Velocity, U_∞	50.8 m/s
Freestream Mach number, M_∞	0.149
Laminar viscosity, μ	$1.80409\cdot10^{-5}$ kg/(s·m)
Reynolds number based on Re_{cref}	1.6 million
Angle-of-Attack (NASA), deg	0.05, 5.28, 10.00, 14.72, 15.76, 16.83, 17.39, 18.96, 19.99, 22.55, 25.09, 30.10
Angle-of-Attack (FOI, DSTO), deg	0.05, 5.28, 10.00, 15.25, 16.28, 17.39, 18.96, 19.99, 21.01, 23.06, 25

6.1.1 Force and Moment Coefficients

Comparisons of experimental lift and pitching moment coefficients with computed results are presented in Figures 6-9. As a general observation of the experimental data [3] in these figures, the C_L and C_m curves are well behaved up to $\alpha\approx16$ deg. Beyond this α range, the pitching moment data exhibits a dramatic reduction between 17 and 18 degrees angle of attack. Beyond the C_m break is an equally sudden restoration of more positive pitching moment. A detailed analysis of the SACCON flow field is presented in Ref. [2]. Some insight into the underlying mechanisms for the observed behaviors is gained by examining the surface flow traces and pressure coefficient contours in Figure 10, which correspond to the USM3D/SA Grid 3 solutions in Figure 6. The benign behavior at the lower angles of attack are confirmed by the stable attached flow streamlines at α=5.28 deg. The remaining three images in Figure 10 depict the surface flow details just before, during, and just after the pitch break. Note the evidence of a stable multiple vortex system at α=16.83 deg, then a sudden forward migration of the outboard leading edge vortex at α=17.89 deg, followed by a full migration and coalescing of the inner and outer vortices at α=18.96 deg. Beyond the pitch break in Figure 6 is a post-stall region for α >20 deg characterized by coalesced vortex structures and vortex breakdown.

6.1.1.1 NASA/USM3D F&M Results

A set of time-accurate static USM3D/SA flow solutions were generated on the four NASA grids (support sting included) from Tables 1 and 2 and in Figure 4 for the twelve angles of attack between 0 and 30 degrees in Table 3. The time step was $\Delta t \approx 0.0002s$ based on a prescribed characteristic time step of $\Delta t^{*}=0.02$ where $\Delta t=\Delta t^{*} \cdot c_{ref}/U_{\infty}$. Solutions were initially advanced in time for 1500 time steps using 5 to 6 inner iterations of the 2nd order physical time step scheme. With the two-equation SST, k-ω, and ARSM turbulence models an additional 750 to 1500 time steps were required for solution convergence beyond α >16 deg. The DES option was not exercised in this study.

The static USM3D/SA solutions on the four NASA grids are compared with the experimental lift and pitching moment coefficients in Figure 6. Up to $\alpha \approx 16$ deg, USM3D compares very well with C_L and with C_m at α=0 deg. Beyond α=0 deg, the C_m is dramatically under predicted. This poor correlation of C_m at lower angles of attack where one might expect better agreement has been a common problem among all of the AVT-161 RANS results [7-13]. A limited exploration of this issue in Ref. [26] suggests that the SA model with an added Rotation Correction (RC) term and Delayed DES (SARC/DDES) results in an increased resolution of unsteady flow separation past the aft-placed support sting that has a stronger-than-expected favorable impact on the pitching moment correlation. This is an example where the inherent dissipation of the RANS formulation produces excessive numerical damping that prevents the development of critical flow features in a sensitive region of the flow.

The observed pitch break between 15 and 20 degrees angle of attack in Figure 6 is also reflected in the USM3D results, albeit more intensely than in the experiment. Beyond the C_m break is an equally sudden restoration of more positive pitching moment that is over predicted by USM3D/SA. Such over prediction of deep-stall flow is typical from the RANS Spalart-Allmaras model due to excessive damping from over production of turbulent viscosity. Another study [13] has suggested that a rotation correction to the SA model can improve this correlation.

In general, the solutions in Figure 6 exhibit some sensitivity to the grid refinement that are most pronounced around the pitch break, and in the deep stall region. It is observed that Grids 1 and 1.1 yield similar results up to the pitch break region. Grids 2 and 3 are in close agreement with each other across the α-range, suggesting grid convergence. Since Grid 2 is considered converged, it will be used in the following assessment of turbulence model sensitivities.

The impact of several RANS turbulence models on Grid 2 is examined using Figure 7, which include results from the Menter SST and Wilcox 1988 k-ω two-equation turbulence models, and two computational results at α=20 deg using the k-ε based non-linear ARSM models from Girimaji and Shi/Zhu/Lumley (SZL). Results show large variations between these turbulence models, much larger than from grid refinement. As before, correlation with experimental data up to $\alpha\approx16$ deg is relatively good for C_L and still poor for C_m, with a slight improvement being offered by the SST model. The turbulence models also result in variation of the pitch-break angle of attack by as much as 2 degrees, and in the severity of the break. The most pronounced effect is in the post-stall region where very large variations are noted. With the exception of the angle of pitch break, the SST model yields the best correlation of all the USM3D turbulence models. However the general prospect of obtaining reasonable correlations of the SACCON pitching moment characteristics from these RANS formulations is not promising.

6.1.1.2 FOI/EDGE F&M Results

Both steady-state RANS and unsteady DES static flow solutions are provided by FOI with the EDGE solver using the FOI Basic and Adapted grids and summarized in Tables 1 and 2 and in Figure 5. The effect of both grid and turbulence model on the integrated forces are shown for the FOI EDGE results in Figure 8. The Basic-grid RANS solution experienced rather strong oscillatory behavior as evidenced by the large error bars. The Adapted-grid RANS and both Basic- and Adapted-grid DES solutions exhibited a much smaller range of oscillation. The general practice was to average the coefficients over the final 200 iterations to establish a mean value. No additional investigation was made regarding the source of the oscillations, but since the grid adaption resulted in substantially less oscillation of the RANS solution, then one might reasonably suspect it to be a grid resolution issue. Hence, the Basic grid does not have adequate resolution for converging RANS solutions.

All of the FOI grids and turbulence models in Figure 8 show similar correlations in the linear region of the C_L curve and wide variation for C_m up to $\alpha=15$ deg. Note that the C_L is predicted slightly lower than the experimental data in this α range. This offset in C_L is due to the absence of the support sting in the geometric representation, as evidenced by the better correlations with sting on in Figure 7. Other partners in the AVT-161 task group have also verified this effect [7-13]. The extremely poor correlation of C_m for the Basic grid below $\alpha=15$ deg again confirms insufficient grid resolution. While the correlation of C_m for the Adapted grid is not satisfactory, as discussed in the previous section the trends are consistent with an absence of the sting and with other RANS solutions.

The correlations between the RANS and DES turbulence models diverge beyond $\alpha > 15$ deg. Consistent with earlier discussion, the Adapted-mesh solutions better capture the predictions and behavior of post-stall lift. Also, the post-stall lift is in close agreement with the experimental data for the time-accurate DES-SA, but the merits of RANS vs. DES are inconclusive for pitching moment. Since the moment reference point (*MRP*) is so far away from the balance instrumentation located at *RRP* in Figure 2, the moment predictions are more sensitive to small variations in the location and extent of the vortices.

6.1.1.3 DSTO/EDGE F&M Results

Steady-state RANS solutions were generated by DSTO on the P3h grid and the four NASA grids summarized in Tables 1 and 2, and in Figures 4 and 5, using the EDGE flow solver with the SAO, SALSA, and Menter SST turbulence models. As a reminder, the P3h grid did not include a model support sting, whereas the NASA grids did. The average y^+_{node} for the P3h mesh in Table 2 is approximately 1.5. The corresponding y^+_{node} for the NASA grids for a node-based solver is estimated to be $4y^+_{cell}$, which is 1.6. Thus, the y^+_{node} values are comparable for between the DSTO and NASA grids for the EDGE solutions, which suggests that any differences in correlation will be related to differences in nodal distribution within the grids and model support sting effects.

The DSTO P3h grid has approximately 3.75-times the number of nodes, twice the number of prisms, and slightly more tetrahedra than the half-span equivalent to the FOI Basic grid in Table 1. However, Figure 5 suggests that a large fraction of P3h nodes are concentrated near the surface, thereby reducing the off-body resolution compared to the FOI Basic grid. The close-up images of the leading edge grid in Figure 5c also indicate large concentrations of nodes near the leading edge of the P3h grid as compared to the Basic grid, which further explains the loss of off-body field resolution. The NASA grids are extremely coarse (0.6 to 2.15 million nodes) for a node-based solver like EDGE, but are included for reference and to address sting effects. Furthermore, the number of nodes for the NASA Grid 3 is comparable to that of the half-span equivalent FOI Basic grid in Table 1.

The DSTO solutions are compared with experimental [3] coefficients of lift and pitching moment in Figure 9. As with prior comparisons, lift is predicted fairly well with the P3h grid up to α=15 deg. The effect of the support sting is most evidenced by an improved correlation with experimental C_L and C_m at α=0 deg for the NASA grid solutions. The slopes of the lift curve for the three P3h-grid solutions are slightly over predicted at the lower angles of attack. The DSTO solutions on the NASA grids, which include the post sting, show improved correlations of lift coefficient up to α=10 deg that are comparable to those from the USM3D solver in Figures 6 and 7.

The DSTO P3h solutions capture approximately half the experimentally measured levels of C_m up to α=15 deg, and significantly over predict the post-stall moments. A correlation of this result with the slightly better result for the FOI Basic grid in Figure 8 strengthen the conclusion that off-body grid resolution is important and is not sufficient to resolve the vortex flow physics with these grids. This inadequate resolution precludes any clear assessment of turbulence model effects using the P3h grid. The correlations of C_m for the EDGE SALSA solutions on the four NASA grids indicate a slight improvement compared to experiment over the lower and higher angle-of-attack ranges, which include an undetermined increment from the post sting. However, these solutions are highly sensitive to grid resolution over the 15 to 20 deg range of angle of attack.

6.1.2 Surface Pressure Distributions

Comparisons of surface pressure coefficient (C_p) distributions at the six stations shown in Figure 3 are presented in Figures 11-14 for $\alpha\approx$17 deg. These stations correspond to three chordwise locations ($x/c_{root}=0.20$, 0.45, and 0.70), two stations normal to the leading edge ($s/LE=0.62$ and 0.94), and one spanwise location ($2y/b=0.26$). Upon examination of the experimental data [3] denoted by open circles, the evidence of vortex flow is apparent over most of the wing at this angle of attack. While not shown, the lower angles of attack are characterized by more attached flow distributions with strong leading-edge suction peaks along the forward portions of the wing. As angle of attack increases, the vortical footprint develops near the tip and progresses forward with increasing angle of attack.

While C_p comparisons are available for all angles of attack in Table 3, only the α=17.89 (NASA) and 17.39 (FOI) deg conditions will be assessed in the following. In general, C_p correlations were relatively good at the lower angles of attack and tend to deteriorate with increasing angle of attack. The selected angle of attack ($\alpha\approx$17 deg) corresponds to the pitch break in Figures 6-9 and represents one of the most challenging conditions to analyze.

6.1.2.1 NASA/USM3D C_p Distributions

The effect of grid refinement on SACCON surface pressure distribution at α=17.89 deg is shown in Figure 11 for USM3D with SA turbulence model. The sensitivity to the four NASA grids is most notable midway back on the wing at stations x/c_{root}=0.70 and s/LE=0.62. In general the finer Grids 2 and 3 are mostly converged. The coarser Grid 1 and its isotropic variant Grid 1.1 neither correlate well with each other nor with Grids 2 and 3. However, the Grid 1.1 does compare slightly better with Grids 2 and 3 than Grid 1 implying that the increased spanwise resolution of the isotropic cells along the leading edge (lower right) has a favorable effect on modeling the leading-edge flow separation.

As a general observation, the computational solutions produce vortex suction peaks that are more pronounced and more outboard than those measured by experiment. A visual correlation of the α=17.89 deg surface C_p contours and flow traces in Figure 10c confirms that the dual suction peaks at $x/c_{root}=0.70$ in Figure 11 are produced by a dual vortex system on the wing. At station $x/c_{root}=0.45$ in Figure 11, the attached flow leading-edge suction peak corresponds approximately with the beginning of the dark blue C_p contours in Figure 10c that indicate the onset of leading-edge flow separation.

The effect of turbulence model on surface pressure is portrayed similarly in Figure 12. The correlations reveal that the SST model more closely follows the experimental result by migrating the suction peak more inboard and reducing its level. Furthermore, the loss of the attached flow suction peak at station $x/c_{root}=0.45$ for the SST model indicates that the leading-edge flow separation has occurred upstream of that station. The SA and k-ω (KOM) models both exhibit similar behavior to each other with strong, outboard suction peaks. NASA's long experience with the SST turbulence model has led to it being the USM3D model of choice for computing separated flows with the RANS approximation. However, the higher-fidelity DES models should be investigated in future USM3D studies of the SACCON wing.

6.1.2.2 FOI/EDGE and DSTO/EDGE C_p Distributions

The sensitivities of SACCON surface C_p distributions at α=17.39 deg to EDGE turbulence models and grid density are examined. Results are presented in Figure 13 for FOI using EDGE RANS/EARSM and DES/SA turbulence models on the FOI Basic- and Adapted-grids, and in Figure 14 for DSTO using EDGE SAO/SST/SALSA turbulence models on the P3h grid. A wide variation of correlation is observed among the models and grids with a variety of peaks and oscillations exhibited in the distributions.

Focusing on the better resolved Adapted-grid results in Figure 13; the RANS (EARSM) solution has many similarities to the USM3D SST solution in Figure 12. While the EDGE/EARSM C_p suction peaks are more pronounced on the forward wing ($x/c_{root}=0.20$ and 0.45), their agreement with the USM3D/SST distributions at the aft stations is nearly identical. The distributions of the Adapted-grid DES-SA solutions appear quite oscillatory, and may require additional averaging over a longer time sample. The corresponding surface C_p contours are also included at the top of Figure 13. The two left images are the Basic-grid RANS and DES result, whereas the two right images are the Adapted-grid RANS and DES result. Note that the locations of separation onset indicated by the beginning of dark blue contours vary significantly. The two Adapted-grid results show this onset location to be ahead of the $x/c_{root}=0.45$ station. Not surprisingly, the corresponding C_p distributions for the under-resolved Basic-grid correlate poorly with experiment. It should be noted that the Basic-grid RANS result represents a snapshot of a highly oscillatory solution since it is plotted without filtering.

The predominant attached-flow like C_p distributions from the DSTO EDGE solutions in Figure 14 is consistent with an under-resolved P3h grid. At station $x/c_{root}=0.70$ the SST and SALSA turbulence models do correctly capture the character of the experimental C_p distribution.

6.1.3 Off-body Flow Field Comparisons

Off-body vorticity contours above the wing are presented in Figure 15 from experimental Particle Image Velocimetry (PIV) measurements [6] of SACCON at $\alpha \approx 17$ deg, followed by similar computational results from NASA, FOI, and DSTO in Figures 16-18, respectively. A thorough flow analysis for the SACCON flow field is presented in Ref. [2], which determined that three vortex systems were present at $\alpha \approx 18$ deg; an apex vortex, a thickness-caused vortex and a leading-edge vortex. This triple vortex system also appears to be present in the PIV data [6] at $\alpha = 16.9$ deg in Figure 15, and is further clarified in Figure 19 at the $x/c_{root}=0.70$ station cut. In Figure 19, the leading-edge vortex is evidenced by the region of strong vorticity (blue) near the leading edge, whereas the two yellow regions of vorticity distinguish the inboard thickness and apex vortices.

The computed off-body vorticity contours in Figures 16-18 provide insight into how well the flow is being modeled and resolved by the respective flow solvers and grids. The vorticity is calculated from the built-in functions of EnSight® using only the cross flow velocities in the y- and z-directions. In general, RANS-based solutions exhibit considerable diffusion that tends to obscure delineation of details within the vortex system. The FOI DES-SA solution in Figure 17b contains more detailed flow structures that indicate a resolution of the triple vortex system.

Additional insight is gained by comparing solutions at the $x/c_{root}=0.70$ station in Figures 20-22 with the PIV data in Figure 19. In general, all of the numerical solutions in Figures 20-22 show higher levels of vorticity than measured in the PIV experiment, particularly for the two inner vortices. The NASA USM3D solutions on Grid 2 in Figure 20 show evidence of the triple vortex system, although the thickness vortex has migrated more outboard than experiment. The FOI-EDGE Basic-grid results in Figure 21a,b indicates a loss of flow structure that is consistent with an under-resolved grid, while the Adapted-grid results in Figure 21c,d indicate the presence of a triple vortex system. The Adapted-grid EARSM (RANS) vorticity contours in Figure 21c appear very similar to the USM3D/SST result in Figure 20b, but with slightly more detail. The FOI/EDGE Adapted-grid DES-SA solution in Figure 21d is rich with structure and vortex locations that look remarkably similar to that of the PIV data in Figure 19. The DSTO-EDGE results in Figure 22 do not show evidence of a multiple vortex system with its three turbulence models. This result is consistent with an observation that the P3h grid is significantly less grid-resolved away from the wing than the NASA Grid 2 or FOI Adapted grids in Figures 4 and 5.

6.2 Dynamic Aerodynamics

Sinusoidal forced oscillation simulations using NASA/USM3D and FOI/EDGE flow solvers have been computed on SACCON. Results will be presented for oscillations in pitch ($\Delta\alpha \approx \pm 5$ deg) about the SACCON rotation reference point, $RRP[x,y,z]=[0.855,0,0]$m for selected angles of attack, α_0, in Table 4. There are no DSTO dynamic solutions using EDGE. However, dynamic computations on the DSTO P3h grid are published in Ref. [13] using the cell-centered COBALT code. Fully turbulent flow was assumed for all computational results. The model support sting is included in the NASA representation, and not included in the FOI and DSTO representations. All force and moment coefficients are integrated over the wing aerodynamic surface (sting excluded) and are referenced to wing area $S_{ref}=0.770\text{m}^2$, chord $c_{ref}=0.479$m, moment reference point, $MRP[x,y,z]=[0.6, 0, 0]$m.

The DNW-NWB experimental [4] and NASA/FOI computational SACCON dynamic force and moment coefficients are plotted against angle of attack in Figures 23-26 for the Cases in Table 4. The dynamic experimental data was measured through forced motion of the wing over many oscillation cycles in the wind tunnel. Measurement uncertainty increases with angle of attack, as evidenced by the wider bands in the experimental data at α_0=15 deg in Figure 23, 24, and 26. These uncertainties can arise from a variety of sources, the most likely being the impact of model vibration on hypersensitive leading edge flow separation.

Table 4: Matrix of dynamic cases for SACCON pitch oscillation study, $\Delta\alpha$=+/-5 deg.

Case	TN2373 [4] run no	MPM	α_0, deg	$\Delta\alpha$, deg	f (Hz)	k	p (Pa)	T (degK)	U_∞ (m/s)	M_∞	μ (10^{-5}) kg/(s·m)	Re 10^6
P1	VN1630-35	6° pitch	5.2	5.3	1.00	0.06	99536	288.7	50.1	0.147	1.7918	1.630
P2	VN1650-55	6° pitch	10.4	5.3	1.00	0.06	99575	289.1	50.0	0.147	1.7937	1.627
P3	VN1680-85	6° pitch	15.6	5.4	3.00	0.18	99581	289.1	50.0	0.147	1.7937	1.625
P5	VN1614-19	15° yaw	15.3	5.1	1.00	0.06	98019	289.1	49.9	0.146	1.7937	1.595

Strong hysteresis of C_m vs. α, and to a lesser degree for C_L vs. α, is observed in Figure 23-26. This hysteresis results from the time lag between cause and effect of evolving transient flow structures, such as vortex core location relative to the upper wing surface, vortex breakdown, and suppression of separated flow, and their resulting aerodynamic influence on the oscillating wing. A typical feature of vortex-dominated flow is the increased initial lift in a pitch up maneuver. If followed by a pitch down maneuver, the breakdown moves downstream again but with a lag in time compared to static data and thus will induce a lower level of lift during the down-stroke.

The shape of the C_m hysteresis, e.g. in Figure 23, exhibits a linear quality at lower angles of attack α_0=5 deg where the flow is fairly benign. These shapes become more distorted and non-linear with increasing angle of attack of the SACCON wing, as evidenced by the results at α_0=15 deg, f=1 and 3Hz. There, SACCON is oscillating through the volatile α range between 10 and 20 deg where the static pitch break occurs in the Figure 6-9, thereby encountering the full range of linear and non-linear aerodynamics. Also note a strong effect of frequency on the shape of the C_m curves at α_0=15 deg between f =1Hz and 3Hz, cases P5 and P3, respectively, that is captured in the computations.

6.2.1 NASA/USM3D Dynamic Results

USM3D is applied with sinusoidal pitch oscillation using the URANS formulation in Figure 23 and 24. These computations were initiated before wind tunnel dynamic data became available, and hence are presented at nominal angles of α_0=5, 10, 15 deg with $\Delta\alpha$=±5 deg. The solutions are computed with Roe's Flux Difference Splitting and no flux limiting, and advanced in time with the 2nd-order subiterative physical time step scheme. Dynamic computations were initiated at each angle of attack by solution restart from the converged time-accurate static solutions. Although the dynamic force and moment coefficients are essentially converged to their periodic solution after the first ¼-pitch cycle, the solutions are continued for two full sinusoidal cycles in this study. However, the initial transients are not included on the plots. The URANS solution exhibits a deterministic quality by converging to a very stable solution, in contrast to the uncertainties of the experimental data as noted earlier. The attached body sting moves with the wing in solid body motion, but is not included in the force and moment integrations.

The USM3D convergence guidelines are developed in Ref. [7]. In general, a well-converged solution is achieved using a total of 36,000 total iterations per pitch cycle. As demonstrated in [7] identical well-converged results can be achieved using 360 steps per cycle with 100 inner iterations ($\Delta t^*=0.290$), 720 steps per cycle with 50 inner iterations ($\Delta t^*=0.145$), or 1440 steps per cycle with 25 inner iterations ($\Delta t^*=0.072$), each totaling to 36,000 solution iterations per pitch cycle.

The sensitivity of USM3D turbulence models is examined in Figure 23. The Menter SST two-equation model is correlated with SA one-equation model on Grid 1 from Table 1 and 2 at nominal angles for each of the four Cases in Table 4. Two pitch cycles were performed at each condition using a combination of 720 time steps per cycle and 50 inner iterations. Note that the experimental data extends to slightly higher angles of attack than the computational solutions, which were computed with nominal angles. As observed in Figure 23, significant differences in shape and levels are evident between the C_m hysteresis curves for the SA and SST models and the experimental data. The shape of the computational curves is in reasonably good agreement with that of experiment at the lower angle of attack α_0=5 deg. The vertical offset of hysteresis loops are related to the static offset of C_m in Figure 7. Any estimation of dynamic stability derivatives from these results will rely solely on the shape of the curves, and will not be affected by an offset. The shape of the curves varies to a much greater extent at the higher angles of attack. For example, the SST model produces a small loop in the C_m curve at α_0=10 deg that is not present in the SA solution or the experimental data. And the shapes of the C_m curves at α_0=15 deg are dramatically different from each other, although the general character of the experimental data is captured. The impact of these shape differences on computing dynamic stability derivatives will be a focus of a 3-year follow-on activity through the NATO/RTO AVT-201 task group. However, the results of Figure 23 illustrate the challenges of constructing and selecting accurate underlying turbulence models based on the URANS formulations, which have an inherent set of limitations for massively separated flows. Additional assessments with other physical models, such as other URANS turbulence models, rotation correction, DES, etc., are needed in the follow-on studies.

The effect of grid refinement is examined using the USM3D/SA model on the four NASA grids in Tables 1 and 2. Two pitch cycles were performed at each condition using a combination of 360 time steps per cycle and 100 inner iterations. The comparisons presented in Figure 24 show some significant sensitivity in dynamic pitching moment due to the grid, particularly at the higher angles of attack where there is no clear characterization of convergence related to grid refinement. However, these differences are notably less than those induced by the turbulence models in Figure 23. Both grid and turbulence model are important and not sufficiently resolved at this time. It is recommended that future investigations initially focus on a search for suitable turbulence models for this class of flows using a reasonable grid before devoting many resources to grid sensitivity studies. Table summarizes the total CPU per cycle requirements on an Intel Xeon® 3GHz cluster for the well converged approach using 360 time steps per cycle with 100 inner iterations.

Table 5: Computer resource requirement for SACCON grid study. USM3D/SA, 360 time-steps/cycle, 100 inner iterations (Well-Converged).

Grid	No. Cells	CPU hrs per cycle
1	3,509,170	480
2	6,302,170	850
3	12,532,040	1900
1.1	9,021,867	1200

6.2.2 FOI/EDGE Dynamic Results

Dynamic SACCON solutions from EDGE version 5.0 are presented in Figure 25 and 26 at the experimental angles in Table 4 for Case P2: f =1Hz, α_0=10.4 deg, $\Delta\alpha$=±5.3 deg, and Case P5: f =1Hz, α_0=15.5 deg, $\Delta\alpha$= ±5.1 deg, respectively, using the Basic FOI grid. The static data are included in Figure 25 and 26 as symbols with dashed line to serve as reference points for understanding the dynamic results (solid lines). The offset in static lift and pitching moment is reflected as an offset in the dynamic runs. The numerical results typically show broader hysteresis curves for C_L and C_m compared to experiment. However, the character of the shapes is generally captured. The very large URANS loop between α=15 to 20.3 deg for Case P5 in Figure 26 simply reflects the difficulty of modeling the region through the pitch break in Figure 8. As a reminder, all FOI static and dynamic simulations lacked the presence of the model support sting, which may account for some of the observed differences in absolute force and moment levels.

A consideration of these results in context to those from USM3D/SA and SST in Figure 23 underscores the challenge of computing dynamic stability characteristics of aircraft in non-linear flow regimes with URANS. The extension to dynamic DES is considerably more expensive due to need for smaller time steps and finer grids. Hence, the urgent question to be answered is: How good is good enough for CFD to adequately characterize dynamic stability derivatives for flight simulation models? As mentioned earlier, this question will be addressed by a follow-on NATO/RTO AVT-201 task group

7.0 SUMMARY

Three independent studies from the United States (NASA), Sweden (FOI), and Australia (DSTO) have been analyzed to assess the current state of unstructured-grid computational fluid dynamic tools and practices for predicting the complex static and dynamic aerodynamic and stability characteristics of a generic 53-degree swept, round-leading-edge UCAV configuration, called SACCON. These studies were performed under a larger cooperative effort involving 19 organizations from 9 countries through the NATO/RTO AVT-161 task group titled “Assessment of Stability and Control Predictions Methods for NATO Air and Sea Vehicles”.

Most of the presented assessments utilized the steady and time-accurate RANS assumption on unstructured grids, with a limited assessment of the DES-SA extension, to explore sensitivities to grids, turbulence models, and the support sting. NASA employed the URANS methodology in the tetrahedral cell-centered TetrUSS/USM3D flow solver on full tetrahedral grids generated with the VGRID advancing-front, advancing-layers code. Both FOI and DSTO provided RANS and DES solutions with the vertex-based FOI/EDGE flow solver on hybrid grids containing prisms/pyramids/tetrahedral grids created with the ICEM CFD^{TM} and FOI/TRITET grid generation tools. Correlations with experimental data were provided for force and moments, surface pressure, and off-body flow measurements.

The vortical flow field over the SACCON with a round leading edge proved extremely difficult to model accurately with current methodologies. As a general rule, the prospect of obtaining reasonable correlations of the SACCON pitching moment characteristics from the RANS formulation is not promising, even for static cases. No one methodology proved superior to the others. Large discrepancies were encountered in predicting pitching moment over the lower angle of attack range where good correlation might be expected. The variations due to turbulence models become quite large at the higher angles of attack where volatile changes occur due to sudden migration of leading-edge separation, and post-stall flows. The dynamic forced-oscillation simulations produced a reasonably good rendering of the SACCON lift and pitching moment hysteresis characteristics. Sensitivities due to grid and turbulence model were still observed, but the general shapes of the curves were remarkably similar to those of experiment.

The primary challenge of predicting the SACCON pitching moment remains unresolved, even across the lower angle of attack range. It is recommended that future studies be more concentrated on the application of higher-fidelity turbulence models, such as DES. Sufficient grid resolution is also critical for success, and care must be taken to adequately resolve the vortical flow field above the wing and separation behind the post support sting. The impact of grid spacing across the boundary layer should also be investigated for sensitivities affecting round leading-edge flow separation.

The NATO/RTO AVT-201 task group will continue exploring these CFD modeling issues on SACCON, and begin developing techniques for extracting dynamic stability derivatives from CFD solutions. This group will attempt to answer the question: How good is good enough for CFD to adequately characterize dynamic stability derivatives for flight simulation models? While currently focused on a generic UCAV configuration, the general technologies produced will clearly benefit the broader aerodynamic and S&C communities.

8.0 ACKNOWLEDGEMENTS

The first author gratefully acknowledges the generous support for this work from the NASA Aviation Safety Program, Integrated Resilient Aircraft Controls project, and the Fundamental Aerodynamics Program, Subsonic Fixed Wing project for the opportunity to participate in the NATO/RTO AVT-161 task group. The second author would like to thank the Swedish Armed Forces for financing the FOI research in this task group. The third author would like to thank NATO for allowing DSTO to make active contributions to research in AVT-161.

Special thanks is also extended to our fellow AVT-161 team members for their synergistic interactions [1-13], and in particular to the excellent experimentalists [3-6] who conceived, designed, built, tested, and produced final data for the SACCON wind tunnel model in a very short time frame. And finally, we are grateful for the excellent leadership of Mr. Andreas Schütte and Prof. Russell M. Cummings in co-chairing AVT-161 and facilitating the exchanges of information between partners.

9.0 REFERENCES

[1] Cummings, R. and A. Schütte, A., “An Integrated Computational/Experimental Approach to UCAV Stability & Control Estimation: Overview of NATO/RTO AVT- 161,” AIAA Paper 2010-4392, June 2010.

[2] Schütte, A., Hummel, D., and Hitzel, S., “Numerical and Experimental Analysis of the Vortical Flow Around the SACCON Configuration,” AIAA Paper 2010-4690, June 2010.

[3] Loeser, T., Vicroy, D., and Schütte, A., “SACCON Static Wind Tunnel Tests at DNW- NWB and 14´x22´ NASA LaRC,” AIAA Paper 2010-4393, June 2010.

[4] Vicroy, D. and Loeser, T., “SACCON Dynamic Wind Tunnel Tests at DNW- NWB and 14´x22´ NASA LaRC,” AIAA Paper 2010-4394, June 2010.

[5] Gilliot, A., “Static and Dynamic SACCON PIV Tests - Part I: Forward Flowfield,” AIAA Paper 2010-4395, June 2010.

[6] Konrath, R., Roosenboom, E., Schröder, A., Pallek, D., and Otter, D., “Static and Dynamic SACCON PIV Tests - Part II: Aft Flow Field,” AIAA Paper 2010-4396, June 2010.

[7] Frink, N., “Strategy for Dynamic CFD Simulation on SACCON Configuration,” AIAA Paper 2010-

4559, June 2010.

[8] Vallespin, D., Boelens, O. and Badcock, K., "SACCON CFD Simulations Using Structured Grid Approaches," AIAA Paper 2010-4560, June 2010.

[9] Tormalm, M. and Schmidt, S., "Computational Study of Static And Dynamic Vortical Flow over the Delta Wing SACCON Configuration Using the FOI Flow Solver EDGE," AIAA Paper 2010-4561, June 2010.

[10] Le Roy, J. "SACCON CFD Static and Dynamic Derivatives Using elsA," AIAA Paper 2010-4562, June 2010.

[11] Chakravarthy S. and Chi, D., "SACCON CFD Simulations Using CFD++," AIAA Paper 2010-4563, June 2010.

[12] Schütte, A., Hummel, D. and Hitzel, S. "Numerical and Experimental Analyses of the Vortical Flow Around the SACCON Configuration," AIAA Paper 2010-4690, June 2010.

[13] Cummings, R. Petterson, K. Jirasek, A. and Schmidt, S., "SACCON Static and Dynamic Motion Flow Physics Simulations Using COBALT," AIAA Paper 2010-4691, June 2010.

[14] Pirzadeh, S. Z., "Three-Dimensional Unstructured Viscous Grids by the Advancing Layers Method," *AIAA Journal*, Vol. 33, No. 1, 1996, pp. 43-49.

[15] Pirzadeh, S. Z., "Advanced Unstructured Grid Generation for Complex Aerodynamic Applications," *AIAA Journal*, Vol. 48, No. 5, 2010, pp. 904-915.

[16] Samareh, J., "GridTool: A Surface Modeling and Grid Generation Tool," Proceedings of the Workshop on Surface Modeling, Grid Generation, and Related Issues in CFD Solutions, NASA CP-3291, 9-11 May, 1995.

[17] ANSYS® ICEM CFD™ User's Manual. http://www.ansys.com/

[18] Tysell, L., "The TRITET Grid Generation System," Proceedings of the 10th ISGG Conference on Numerical Grid Generation, Forth, Crete, Greece 2007 Society of Grid Generation (ISGG).

[19] Frink, N. T., "Tetrahedral Unstructured Navier-Stokes Method for Turbulent Flows," *AIAA Journal*, Vol. 36, No. 11, 1998, pp. 1975-1982.

[20] Frink, N. T., Pirzadeh, S. Z., Parikh, P. C., Pandya, M. J., and Bhat, M. K., "The NASA Tetrahedral Unstructured Software System (TetrUSS)," *The Aeronautical Journal*, Vol. 104, No. 1040, 2000, pp. 491-499.

[21] Pandya, M.J., Frink, N.T., Abdol-Hamid, K.S., and Chung, J.J., "Recent Enhancements to USM3D Unstructured Flow Solver for Unsteady Flows," AIAA Paper 2004-5201, August 2004.

[22] Pandya, M. J., Abdol-Hamid, K. S., and Frink, N. T., "Enhancement of USM3D Unstructured Flow Solver for High-Speed high-Temperature Shear Flows," AIAA Paper 2009-1329, January 2009.

[23] Eliasson, P., “Edge, a Navier-Stokes Solver for Unstructured Grids,” Proc. To Finite Volumes for Complex Applications III, ISBN 1 9039 9634 1, pp.527-534, 2002.

[24] Wallin, S. and Johansson, A. V., “An Explicit Algebraic Reynolds Stress Model of Incompressible and Compressible Flows,” *J. Fluid Mech*., Vol 403, 2000, pp. 89-132.

[25] Rung, T., Bunge, U., Schatz, M., and Thiele, F., “Restatement of the Spalart-Allmaras Eddy-Viscosity Model in Strain-Adaptive Formulation,” *AIAA Journal*, Vol. 41, No. 7, 2003, pp. 1396-1399.

[26] Jirasek, A. and Cummings, R.M., “SACCON Static and Dynamic Motion Flow Physics Simulations Using COBALT,” AIAA Paper 2011-3965, June 2011.

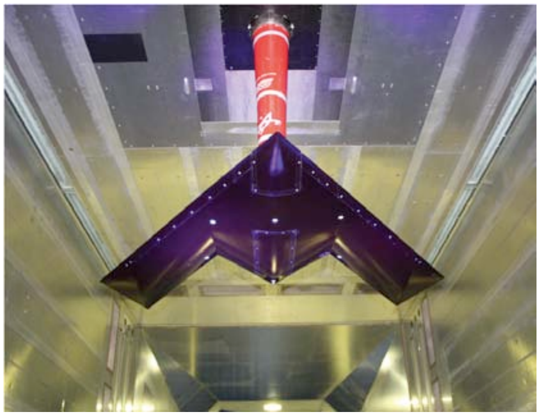

Figure 1 SACCON low-speed wind tunnel model inverted in the dynamic Model Postitioning Mechanism in the closed test section of the Low-Speed Wind Tunnel Braunschweig (DNW-NWB).

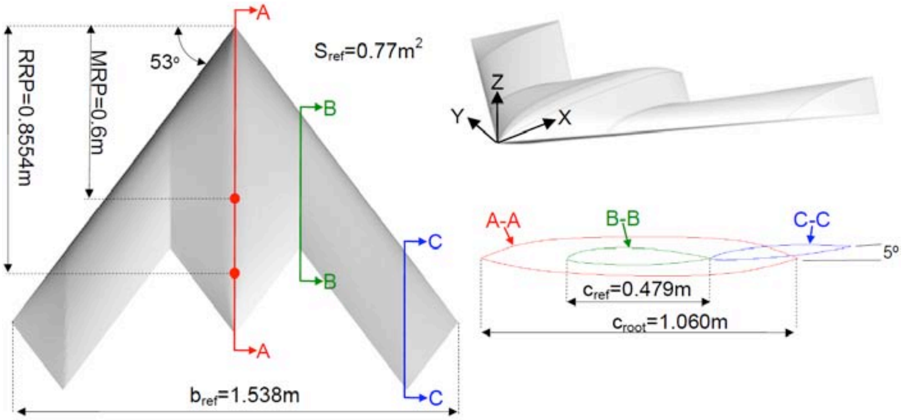

Figure 2 Planform and geometric parameters of the SACCON configuration.

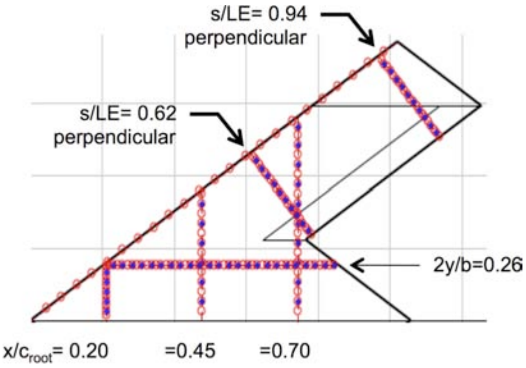

Figure 3 Location of SACCON pressure orifices. UPPER surface – red open circles. LOWER surface – blue dots.

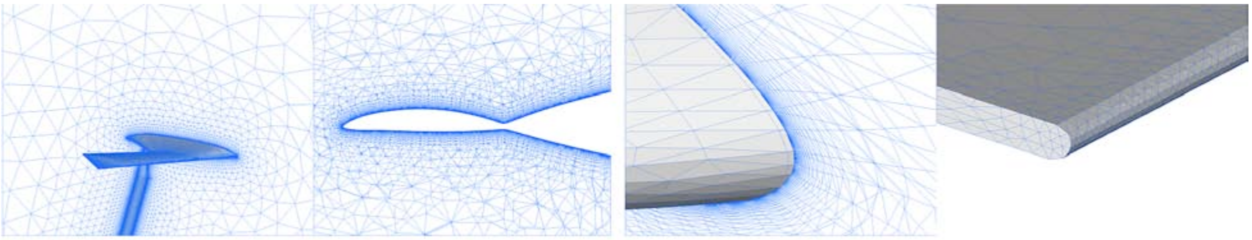

(a) NASA Grid 1

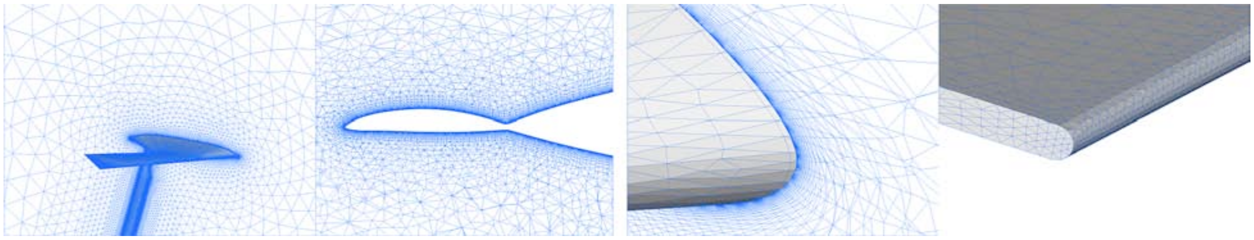

(b) NASA Grid 2

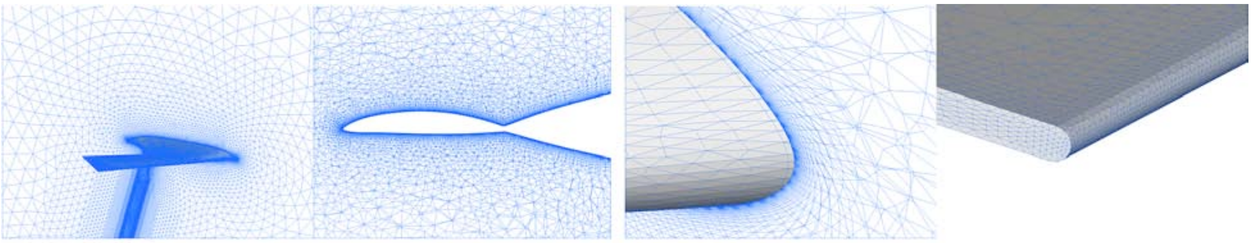

(c) NASA Grid 3

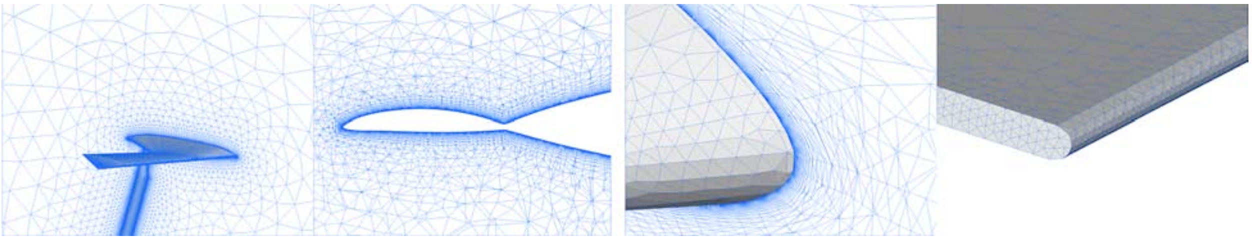

(d) NASA Grid 1.1

Figure 4 Set of four NASA half-span grids. NASA VGRID. From left-to-right: ¾-view of wing with post support sting, cut through volume grid at x/c=0.70, close-up of wing-apex/symmetry-plane juncture, close-up of wing tip leading edge.

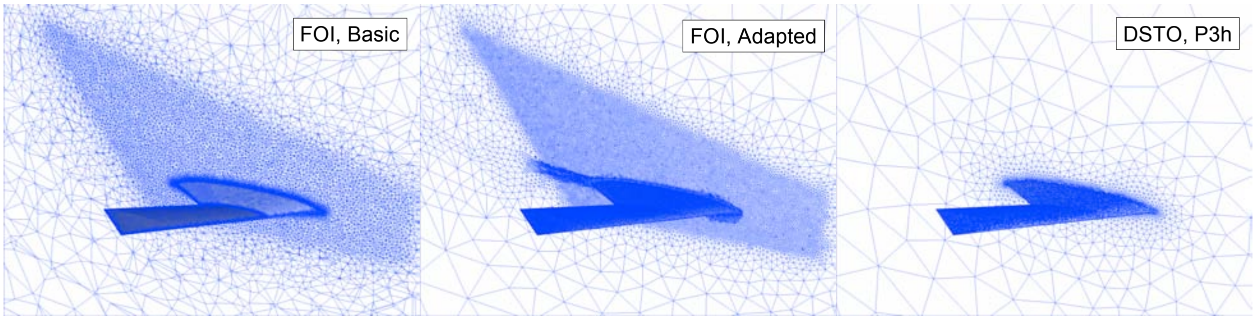

(a) 3/4-view of symmetry plane and wing surface triangulation

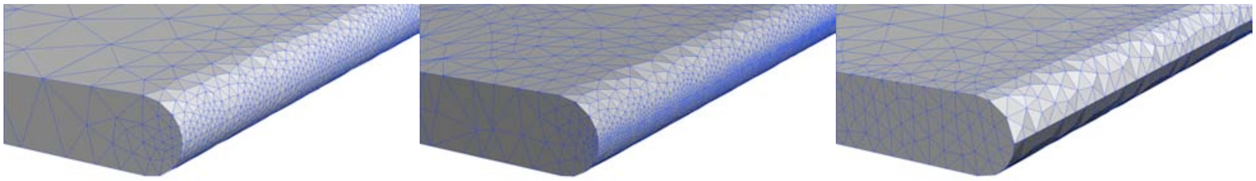

(b) Close-up of wing tip leading edge

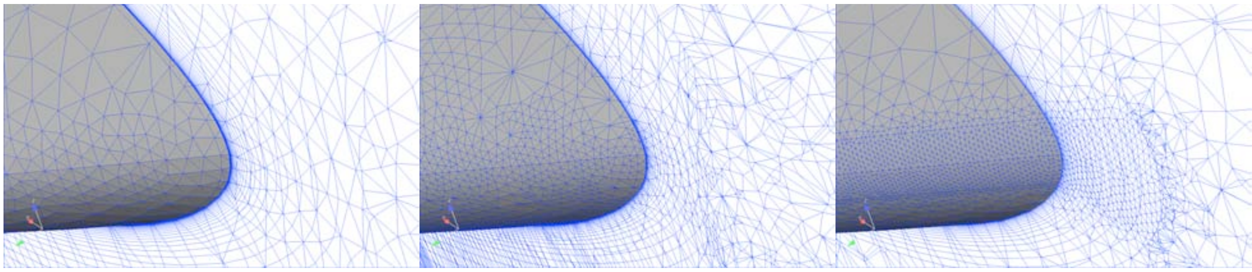

(c) Spanwise cut at y=219mm (B-B in Figure 2)

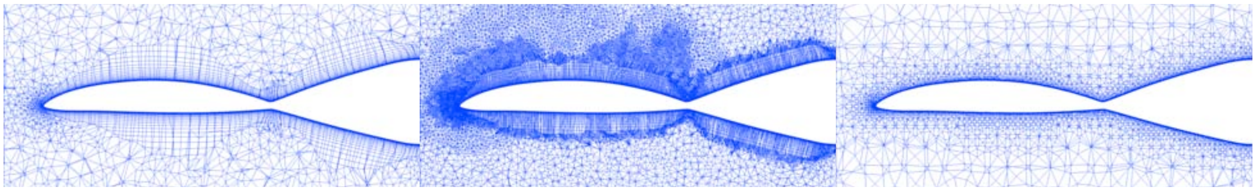

(d) Cut through volume grid at x/c=0.70

Figure 5. Comparison of SACCON FOI Basic full-span mesh (left), FOI solution Adapted half-mesh (center), and DSTO P3h half-span mesh (right). FOI ICEM/TRITET/PRISM.

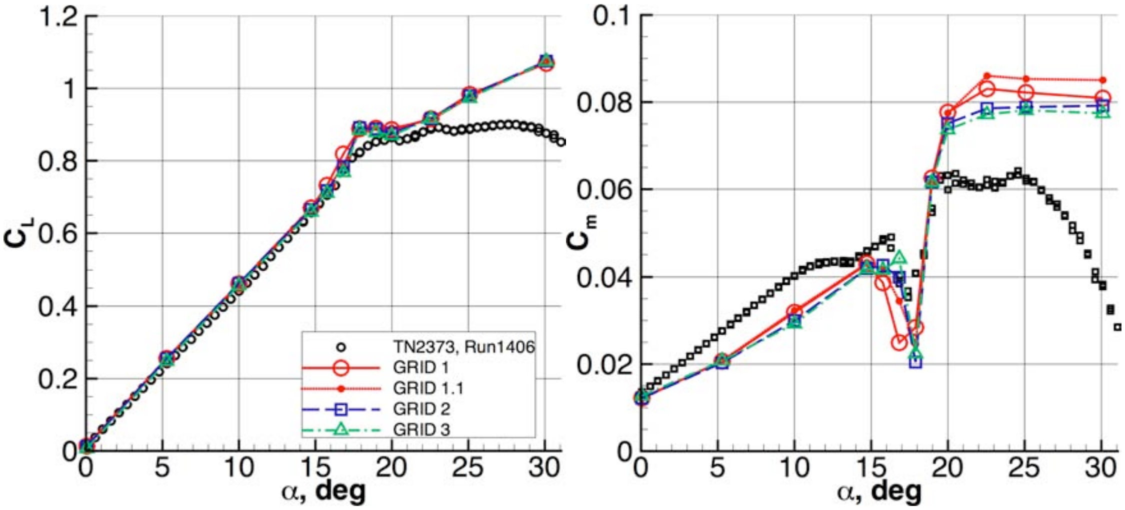

Figure 6 Effect of grid refinement on SACCON static lift and pitching moment coefficient. M_∞=0.144, Re_{cref}=1.6 million. NASA-USM3D/SA.

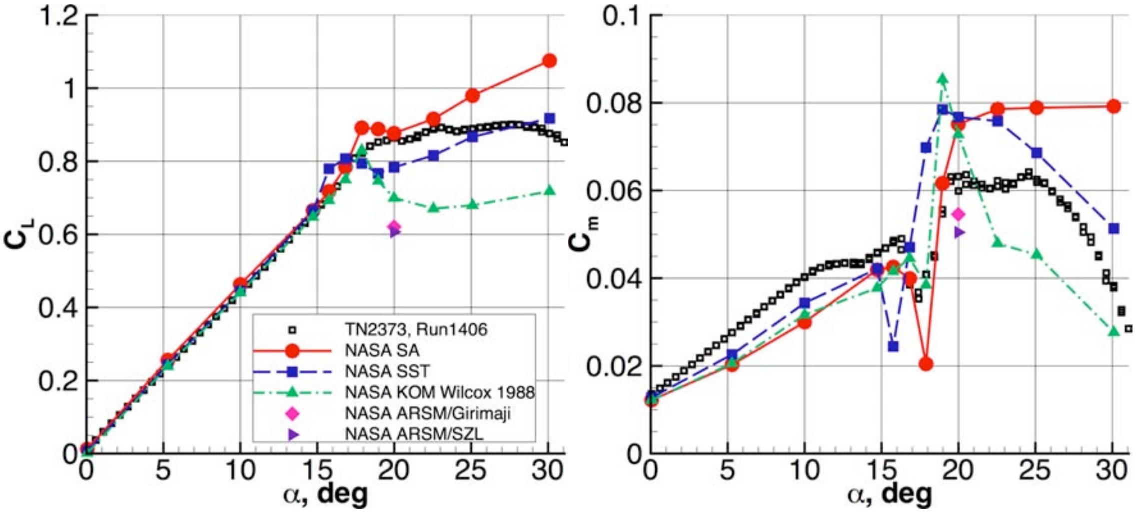

Figure 7 Effect of turbulence model on SACCON static lift and pitching moment coefficient. M_∞=0.144, Re_{cref}=1.6 million. NASA-USM3D, Grid 2.

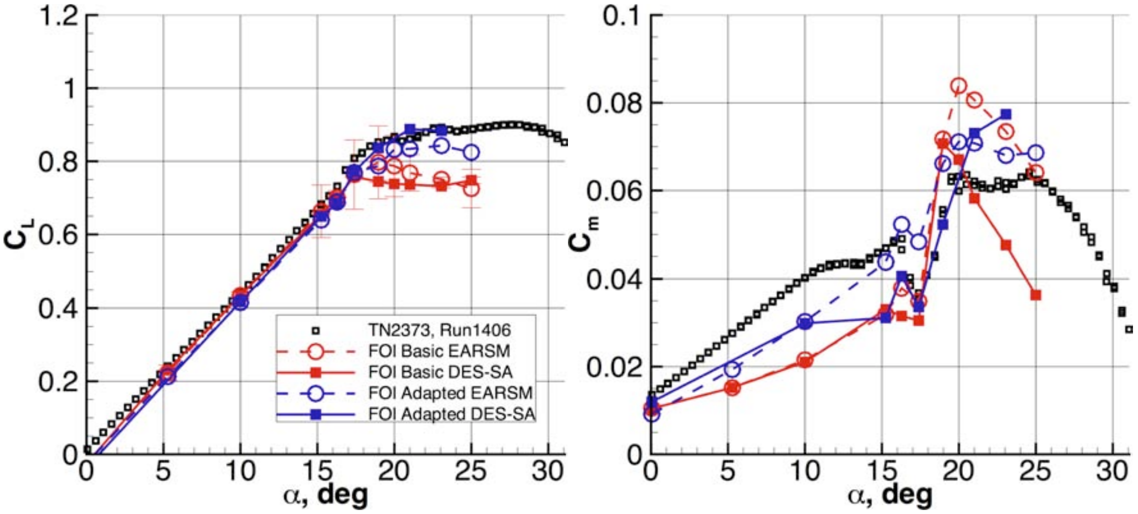

Figure 8 Effect of grid and turbulence model on SACCON static forces and pitching moment coefficients. M_∞=0.149, Re_{cref}=1.6 million. FOI-EDGE.

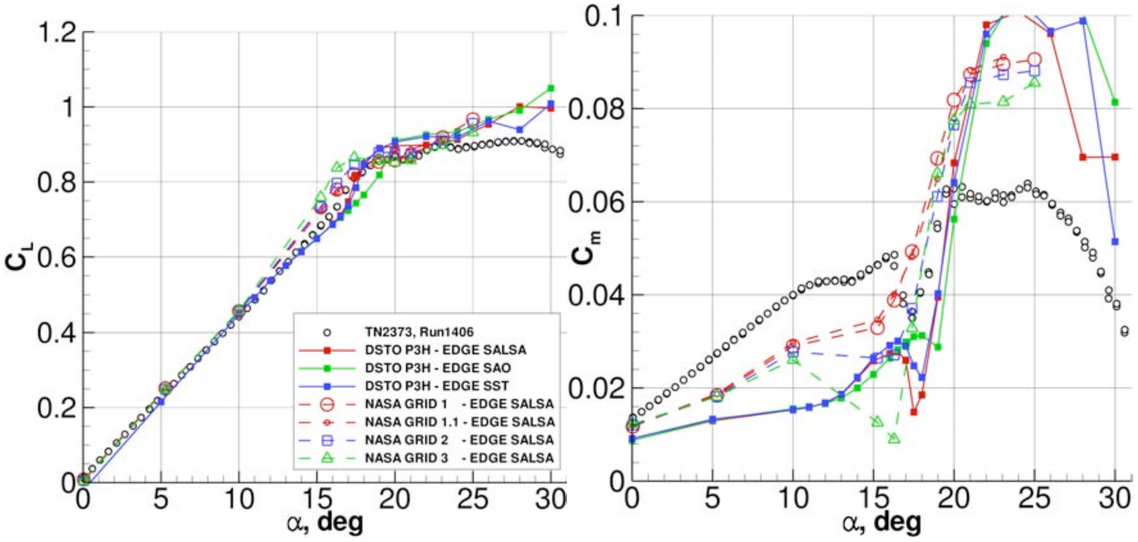

Figure 9 Effect of grid and turbulence model on SACCON forces and pitching moment coefficients. M_∞=0.149, Re_{cref}=1.6 million. DSTO-EDGE.

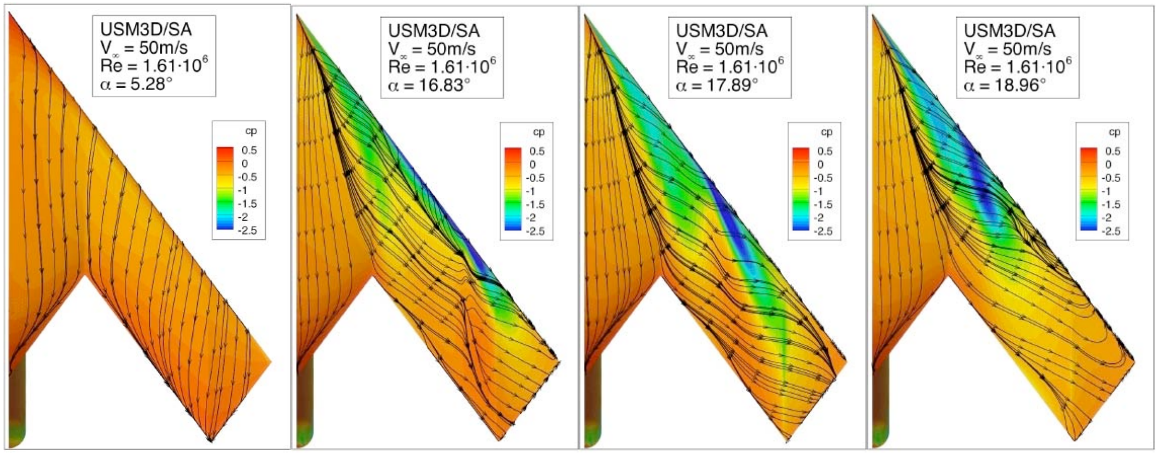

(a) Attached flow (b) just before C_m break (c) during C_m break (d) just after C_m break

Figure 10 SACCON surface Cp contours and flow traces on NASA 12M cell Grid 3. M$_\infty$=0.144, Re$_{cref}$=1.6 million. NASA USM3D/SA.

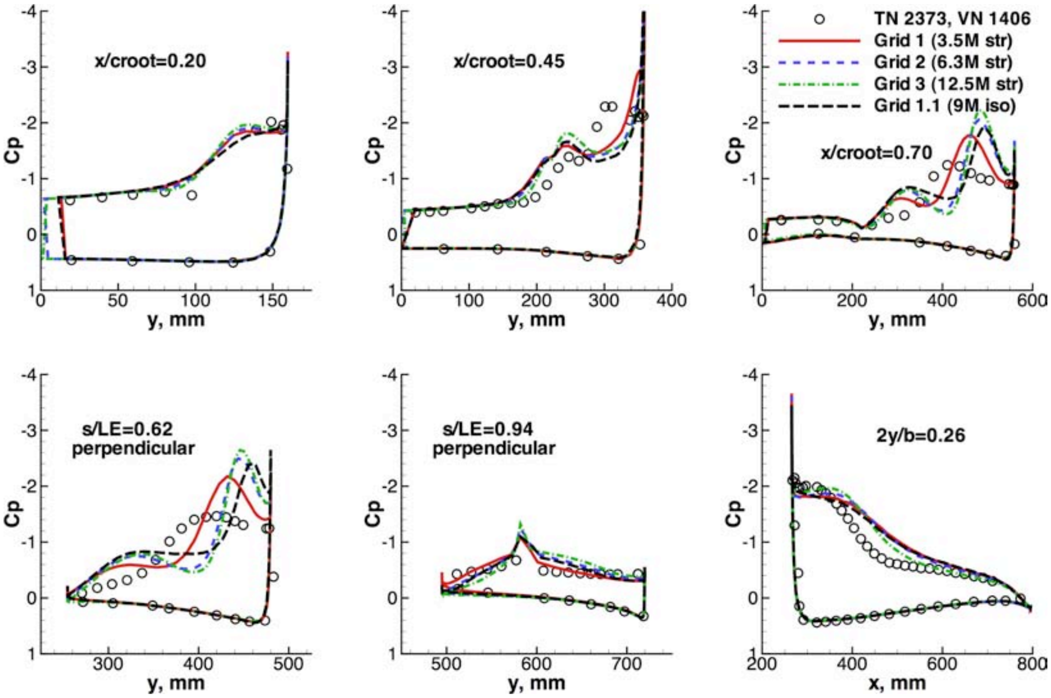

Figure 11 Effect of grid refinement on SACCON surface pressure coefficient. M$_\infty$=0.144, α=17.89 deg, Re$_{cref}$=1.6 million. NASA-USM3D/SA.

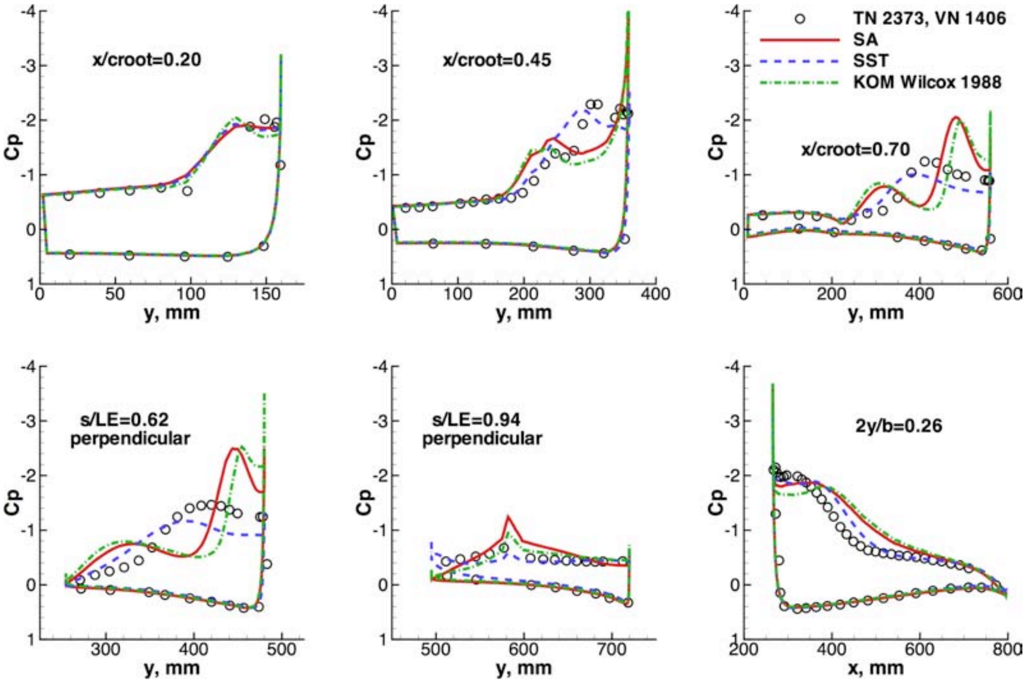

Figure 12 Effect of turbulence model on SACCON surface pressure coefficient. M_∞=0.144, α=17.89 deg, Re_{cref}=1.6 million. NASA-USM3D, Grid 2.

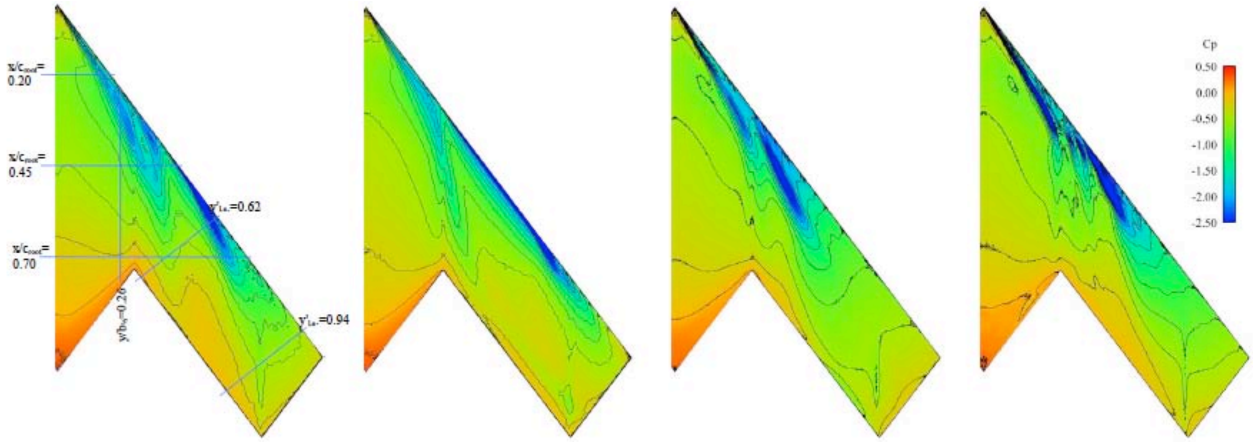

(a) Basic RANS (b) Basic DES (c) Adapted RANS (d) Adapted DES

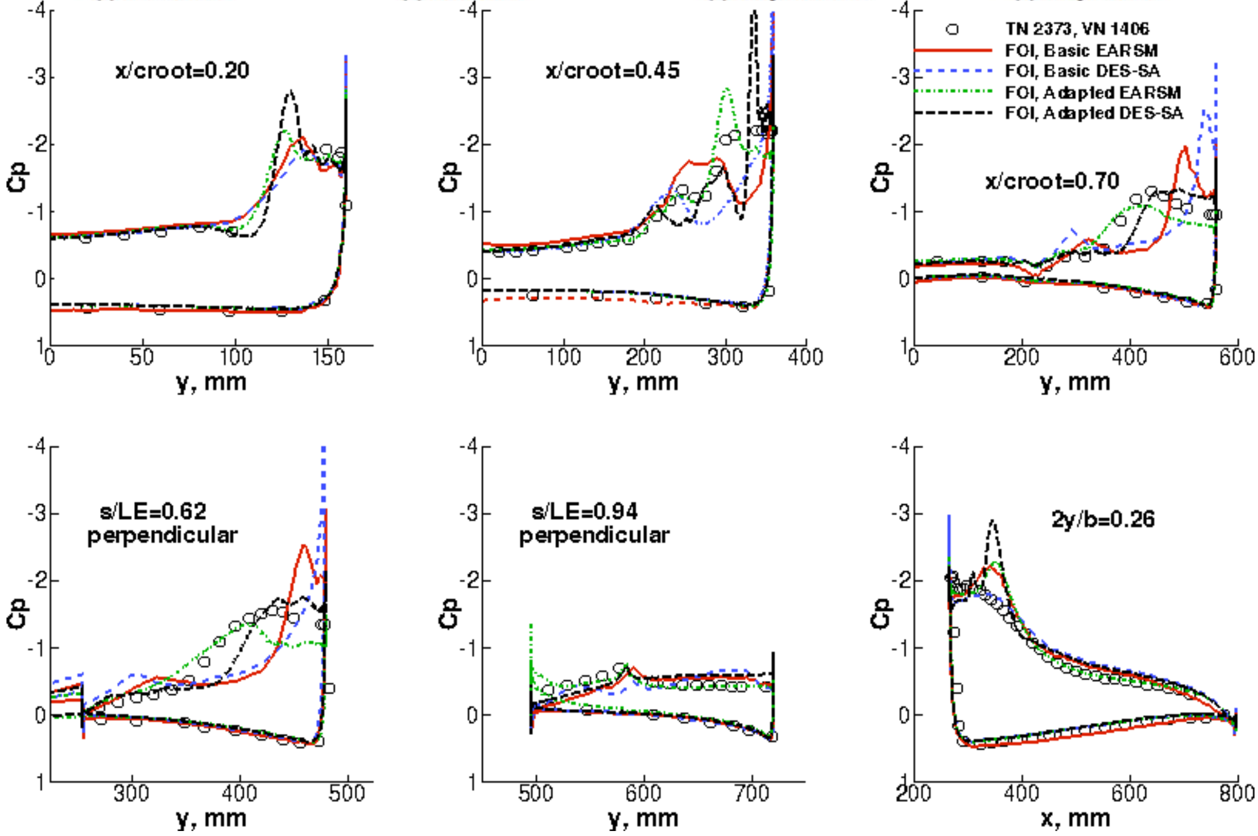

Figure 13 Effect of grid refinement and turbulence model on SACCON surface pressure coefficient. M_∞=0.149, α=17.39 deg, Re_{cref}=1.6 million. FOI-EDGE.

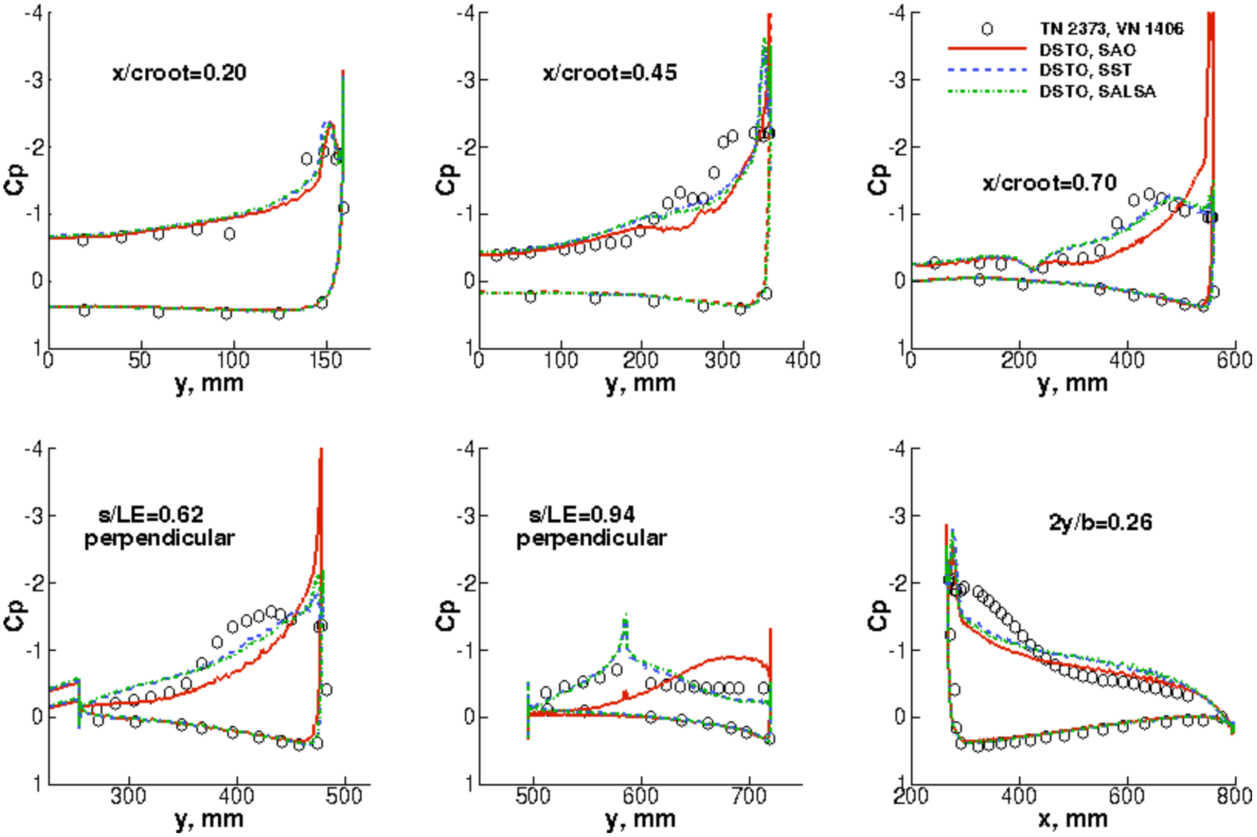

Figure 14 Effect of turbulence model on SACCON surface pressure coefficient. M_∞=0.149, α=17.39 deg, Re_{cref}=1.6 million. DSTO-EDGE, P3h grid.

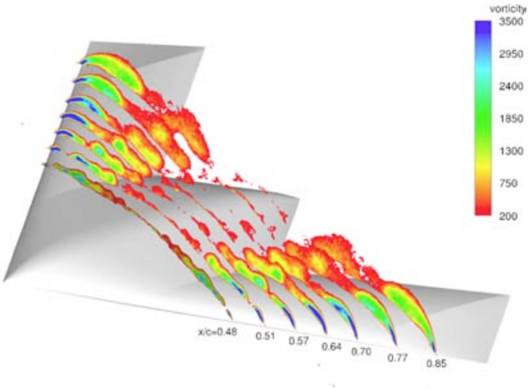

Figure 15 DLR-PIV data [6] for comparison of off-body vorticity contours on SACCON. M_∞=0.149, α=16.9 deg, Re_{cref}=1.6 million.

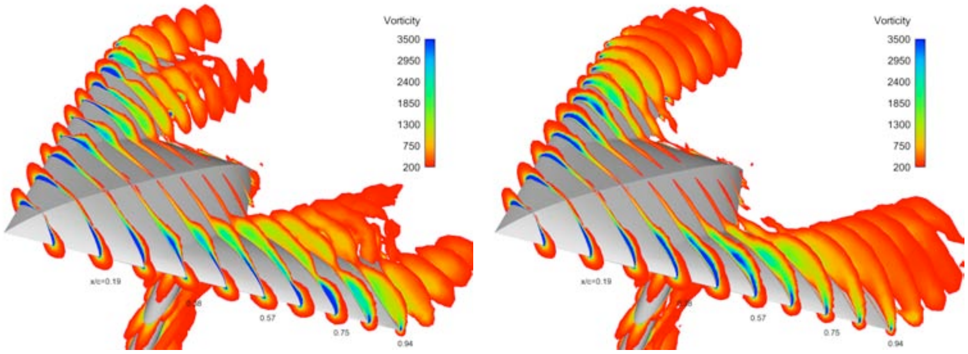

(a) SA turbulence model (b) SST turbulence model

Figure 16 NASA off-body vorticity contours. USM3D, Grid 2. M_∞=0.144, α=16.83 deg, Re_{cref}=1.6 million.

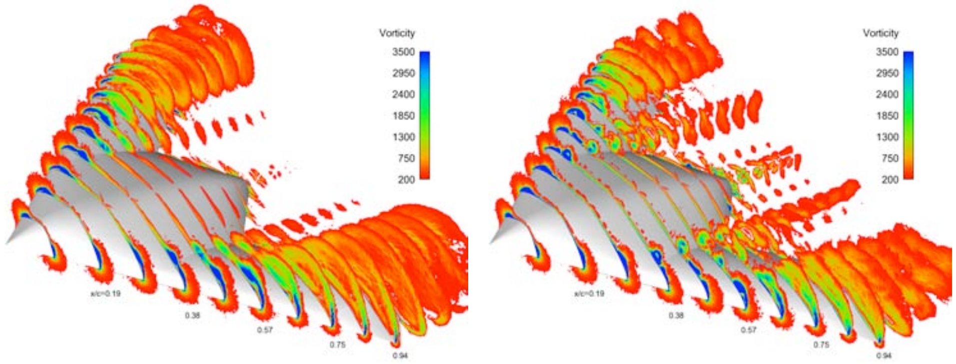

(a) EARSM turbulence model (b) DES-SA turbulence model

Figure 17 FOI off-body vorticity contours. FOI-EDGE, Adapted grid. M_∞=0.149, α=17.39 deg, Re_{cref}=1.6 million.

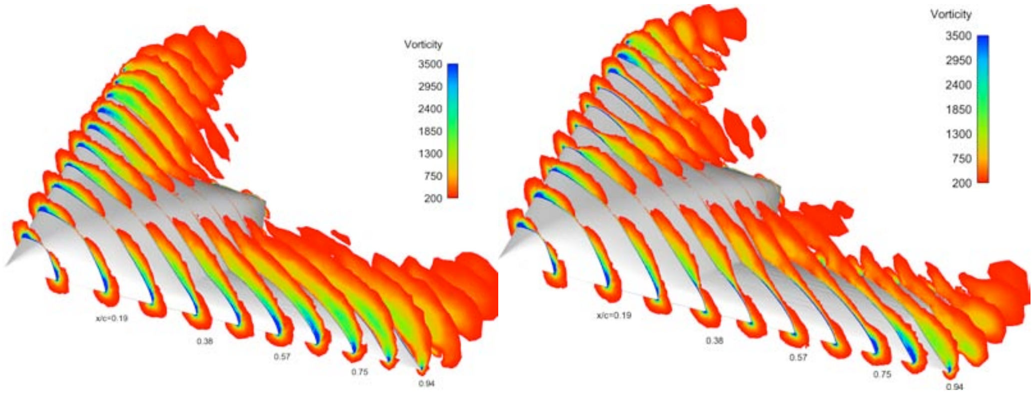

(a) SALSA turbulence model (b) SAO turbulence model

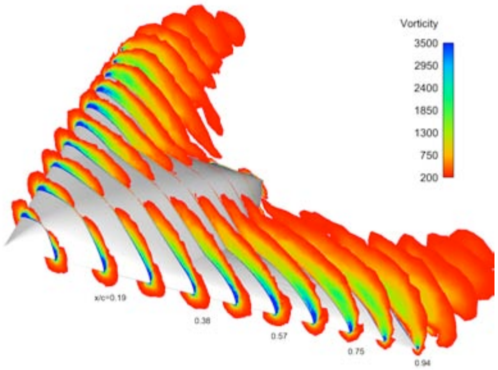

(c) SST turbulence model

Figure 18 DSTO off-body vorticity contours. DSTO-EDGE, P3h grid. M_∞=0.149, α=17.39 deg, Re_{cref}=1.6 million.

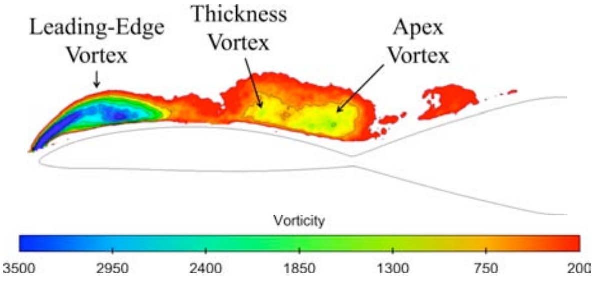

Figure 19 DLR-PIV SACCON data [6] for comparison of off-body vorticity contours at x/c_{root}=0.70. M_∞=0.149, α=16.9 deg, Recref=1.6 million.

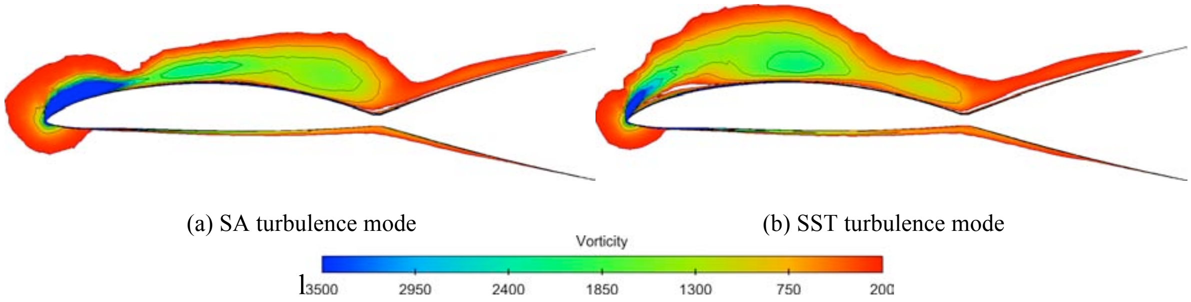
(a) SA turbulence mode

(b) SST turbulence mode

Figure 20 NASA SACCON vorticity contours on SACCON at x/c_{root}=0.70. USM3D, Grid 2. M_∞=0.144, α=16.83 deg, Re_{cref}=1.6 million.

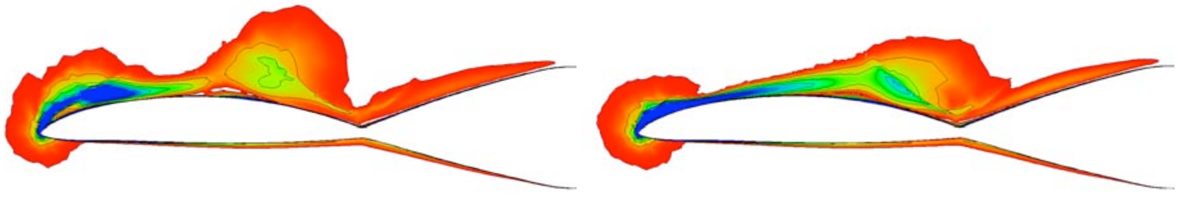
(a) Basic-grid EARSM

(b) Basic-grid DES-SA

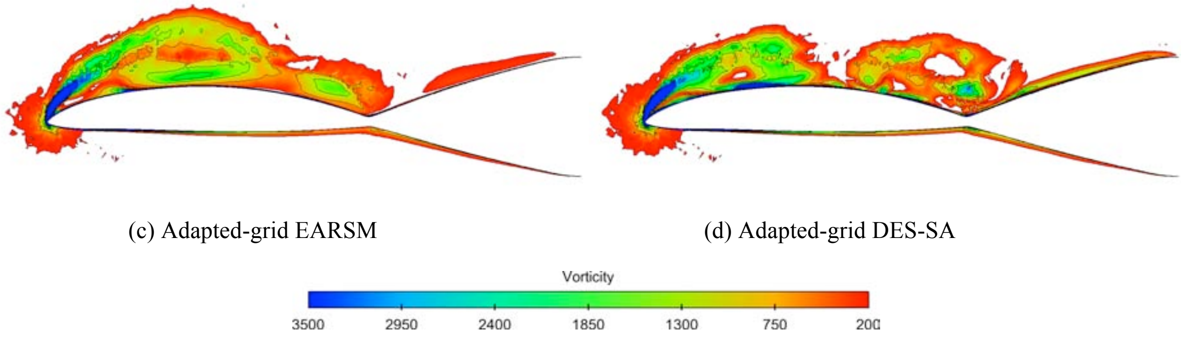
(c) Adapted-grid EARSM

(d) Adapted-grid DES-SA

Figure 21 FOI SACCON vorticity contours on SACCON at x/c_{root}=0.70. FOI-EDGE. M_∞=0.149, α=17.39 deg, Re_{cref}=1.6 million.

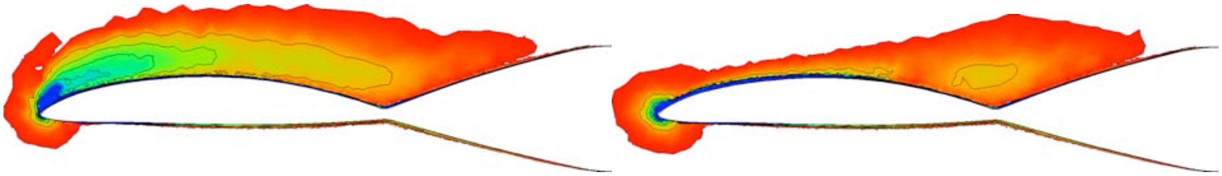

(a) SALSA turbulence mode

(b) SAO turbulence model

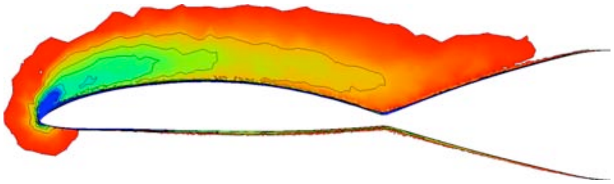

(c) SST turbulence model

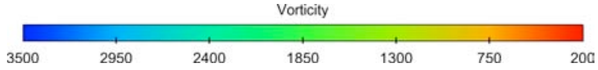

Figure 22 DSTO SACCON vorticity contours at x/c_{root}=0.70. DSTO-EDGE, P3h grid. M_∞=0.149, α=17.39 deg, Re_{cref}=1.6 million.

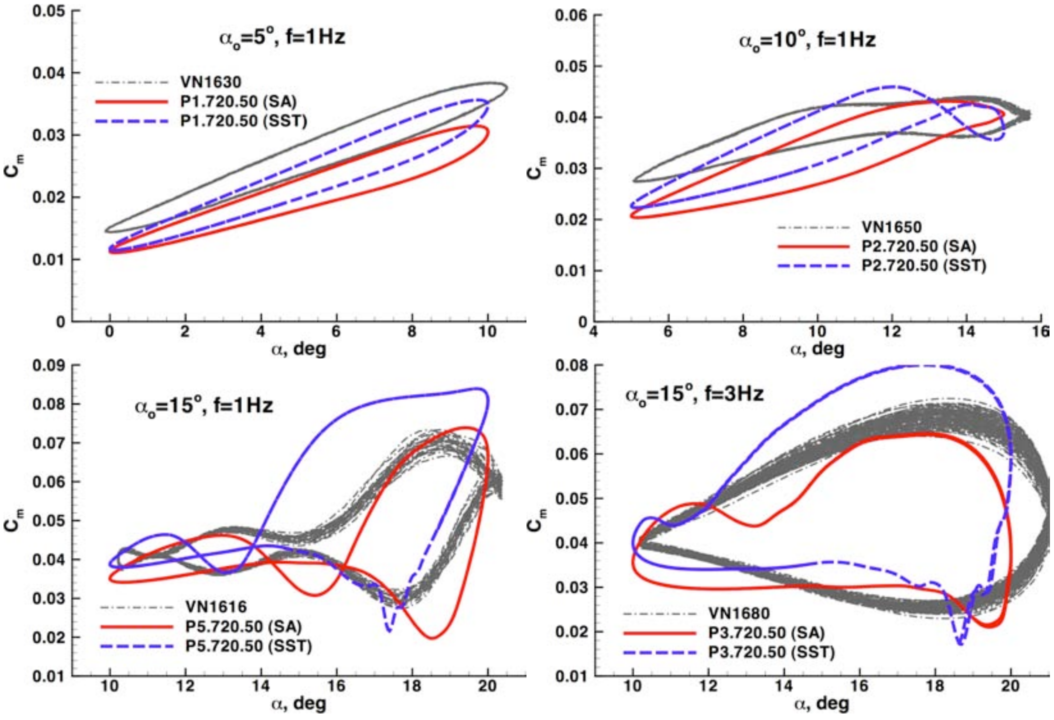

Figure 23 Effect of turbulence model on SACCON dynamic pitching moment coefficient. Cases P1, P2, P5, and P3. M_∞=0.144, Re_{cref}=1.6 million, $\Delta\alpha$=+/-5 deg. NASA-USM3D, Grid 1.

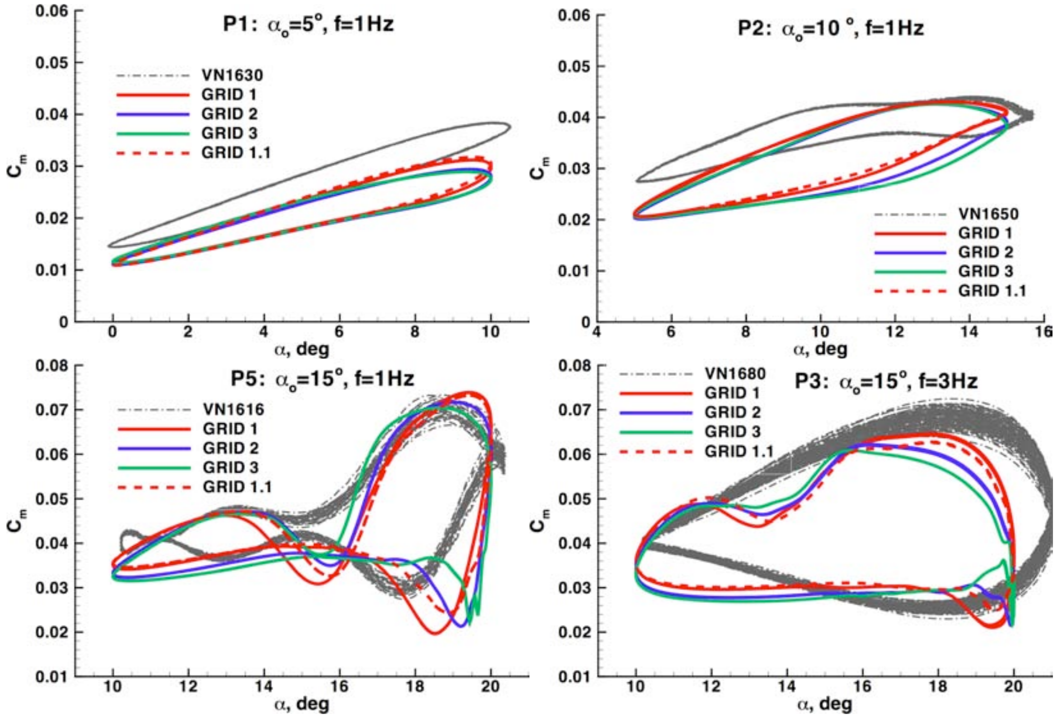

Figure 24 Effect of grid refinement on SACCON dynamic pitching moment coefficient. M_∞=0.144, Re_{cref}=1.6 million, $\Delta\alpha$=+/-5 deg. Cases P1, P2, P5, and P3. NASA-USM3D/SA.

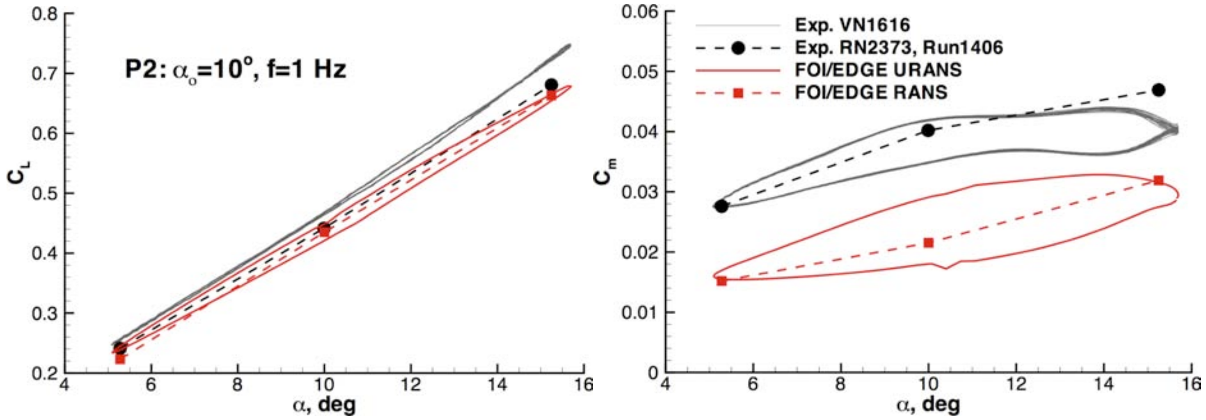

Figure 25 FOI-EDGE/EARSM simulation of SACCON static and dynamic lift and pitching moment coefficients. FOI Basic grid. Case P2: M_∞=0.149, Re_{cref}=1.6 million, α=10.4 deg, $\Delta\alpha$=+/-5.3 deg, f=1.0 Hz.

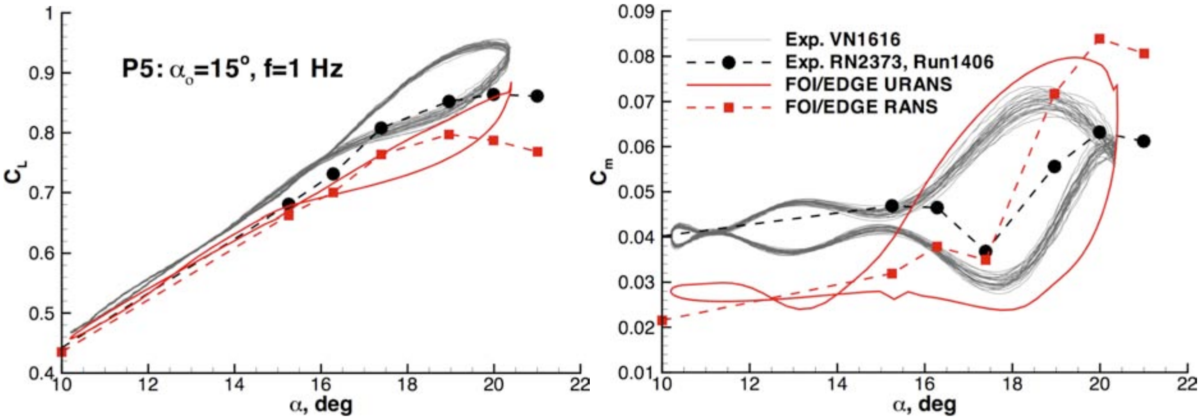

Figure 26 FOI-EDGE/EARSM simulation of SACCON static and dynamic lift and pitching moment coefficients. FOI Basic Grid. Case P5: M_∞=0.149, Re_{cref}=1.6 million, α=15.3 deg, $\Delta\alpha$=+/-5.1 deg, f=1.0 Hz.